

Event-horizon-scale Imaging of M87* under Different Assumptions via Deep Generative Image Priors

BERTHY T. FENG,¹ KATHERINE L. BOUMAN,¹ AND WILLIAM T. FREEMAN^{2,3}

¹*California Institute of Technology (Caltech)*

²*Massachusetts Institute of Technology (MIT)*

³*Google Research*

ABSTRACT

Reconstructing images from the Event Horizon Telescope (EHT) observations of M87*, the supermassive black hole at the center of the galaxy M87, depends on a prior to impose desired image statistics. However, given the impossibility of directly observing black holes, there is no clear choice for a prior. We present a framework for flexibly designing a range of priors, each bringing different biases to the image reconstruction. These priors can be weak (e.g., impose only basic natural-image statistics) or strong (e.g., impose assumptions of black-hole structure). Our framework uses Bayesian inference with score-based priors, which are data-driven priors arising from a deep generative model that can learn complicated image distributions. Using our Bayesian imaging approach with sophisticated data-driven priors, we can assess how visual features and uncertainty of reconstructed images change depending on the prior. In addition to simulated data, we image the real EHT M87* data and discuss how recovered features are influenced by the choice of prior.

1. INTRODUCTION

In 2019, the Event Horizon Telescope (EHT) Collaboration obtained the first picture of M87* through computational imaging methods (Collaboration et al. 2019a,b,c). The published images gave humans a glimpse of the shadow cast by the supermassive black hole (Luminet 1979; Falcke et al. 1999; Lu et al. 2014) in the galaxy M87 based on data that EHT telescopes had collected in April 2017 (Collaboration et al. 2019d,e), and more recent images showed the persistence of the shadow one year later (Akiyama et al. 2024). However, these images necessarily incorporated imaging assumptions that were independent of telescope data. Because measurements obtained from very-long-baseline interferometry (VLBI) (van Cittert 1934; Thompson et al. 2017) with EHT telescopes are corrupted and limited in number, infinitely many images — many of them implausible and not interpretable — would agree with a given set of measurements. Therefore, reconstructing an image from VLBI data requires assumptions about plausible image statistics in order to constrain the space of possible images (Collaboration et al. 2019b).

Imaging assumptions can be formalized as a *prior*, or a probability distribution of images that are acceptable regardless of observations (Scales & Tenorio 2001). More formally, we define a prior as a distribution of images \mathbf{x} with a probability density function $p(\mathbf{x})$. In Bayesian inference the prior helps determine the image posterior $p(\mathbf{x} | \mathbf{y})$ given observations \mathbf{y} . However, designing a prior is not a straightforward task, especially considering the absence of true images of black holes. We address this problem with a principled strategy: we collect a range of priors that each impose different visual biases and plug these priors into a Bayesian imaging algorithm along with EHT VLBI data. Whereas the EHT Collaboration explored different imaging assumptions via the use of different imaging pipelines (e.g., CLEAN (Högbom 1974; Schwarz 1978; Clark 1980; Schwab 1984; Cornwell et al. 1999; Shepherd 2011; Müller & Lobanov 2023) and regularized maximum-likelihood (RML) methods (Bouman et al. 2016; Chael et al. 2016; Akiyama et al. 2019)), we explore different priors within the same imaging pipeline. Our imaging approach allows us to assess how visual characteristics and uncertainty, as quantified through a Bayesian posterior, vary with the choice of prior.

An aim of our method is to easily move along the spectrum between strong constraints and weak constraints on the image. On one side of the spectrum lie model-fitting strategies, which find the parameters of an underlying geometric

(Collaboration et al. 2019c; Vincent et al. 2021; Nalewajko et al. 2020; Lockhart & Gralla 2022; Sun et al. 2022), physical (Collaboration et al. 2019f; Walsh et al. 2013; Gebhardt et al. 2011; Kawashima et al. 2021; Yuan et al. 2022; Nemmen 2019), or statistical (Medeiros et al. 2023) model that best match the observations. On the other side lie traditional imaging approaches using weak regularizers like total variation (Akiyama et al. 2017; Kuramochi et al. 2018) and maximum entropy (Narayan & Nityananda 1986). However, each side has its own limitations: model-fitting prevents discovering new features that cannot be explained by the assumed model, whereas traditional regularizers struggle to produce visually rich images. This motivates a method for imaging under a diverse array of priors, ranging from those akin to model-fitting (e.g., by assuming black-hole structure) to those similar to weak regularizers (e.g., by assuming basic properties of natural images). One can in principle obtain different priors by changing the regularization function (Müller et al. 2023) or tuning regularization parameters (Collaboration et al. 2019b), but it is impractical to hand-design a regularizer for every desired prior.

A promising avenue is to use a data-driven prior that is fit to a training set of images with the desired statistics. Parameterizing the data-driven prior to be expressive enough is crucial. For example, principal components analysis (PCA) offers a simple probabilistic model of images, but it has been shown to not accurately express complicated image distributions (Feng et al. 2023). We choose to parameterize the prior by a score-based diffusion model (*score-based prior*), which has been demonstrated as a powerful deep generative model capable of modeling a variety of image probability distributions (Song et al. 2021b; Ho et al. 2020; Dhariwal & Nichol 2021), no matter how simple or complicated. That is, given a desired image prior $p(\mathbf{x})$, it can be assumed that the learned prior $p_\theta(\mathbf{x})$ with parameters θ trained on samples from $p(\mathbf{x})$ satisfies $p_\theta(\mathbf{x}) \approx p(\mathbf{x})$ (Feng et al. 2023).

With score-based priors, we achieve a collection of M87* images that all fit the observed data but differ in certain visual characteristics. Specifically, we trained a score-based prior on each of the following datasets: CIFAR-10 (Krizhevsky & Hinton 2009) (generic natural images), general relativistic magneto-hydrodynamic (GRMHD) simulations (Wong et al. 2022), radially inefficient accretion flow (RIAF) simulations (Broderick et al. 2011), and CelebA (Liu et al. 2015) (celebrity faces). We use a Bayesian imaging technique to apply each prior to the M87* observations, resulting in a collection of image posteriors. Each posterior is a probability distribution of images conditioned on the M87* data but incorporating a different prior. The visual biases of images from different posteriors are strikingly different, yet the images share structure that is prior-invariant, such as the ring shape and brightness asymmetry. We thus present two contributions based on our results: (1) a collection of possible M87* images that humans can selectively interpret based on their trust of the assumed biases and (2) analysis of which extracted black-hole features are robust to the prior and can be reliably used in scientific analysis.

In this manuscript, we first describe relevant background in Sec. 2 and our Bayesian imaging method involving score-based priors in Sec. 3. In Sec. 4, we present image posteriors of M87* based on a collection of score-based priors ranging from weak biases (e.g., a prior trained on generic natural images) to strong biases (e.g., a prior trained on RIAF images). In Sec. 5, we validate the imaging approach on simulated data. Next, in Sec. 6, we analyze the influence of the prior on characteristic ring features, including diameter, width, and orientation, by performing tests on both the simulated-data and M87* images. Finally, in Sec. 7, we summarize our findings and conclude that our proposed imaging strategy allows one to define any collection of priors and analyze their effect on reconstructed images.

2. BACKGROUND

2.1. Bayesian imaging

Given measurements $\mathbf{y} = \mathbf{f}(\mathbf{x}^*)$, where \mathbf{f} is a known forward model and \mathbf{x}^* is an unknown source image, we would like to recover an image \mathbf{x} such that $\mathbf{f}(\mathbf{x}) \approx \mathbf{y}$. However, when \mathbf{y} is sparse and corrupted, there is inherent uncertainty in the inverse problem of finding \mathbf{x} (Scales & Tenorio 2001). Bayesian imaging accounts for this uncertainty by modeling a probability distribution known as the *posterior*, or $p(\mathbf{x} | \mathbf{y})$. According to Bayes' rule, the log-probability of an image under the posterior is given by

$$\log p(\mathbf{x} | \mathbf{y}) = \log p(\mathbf{y} | \mathbf{x}) + \log p(\mathbf{x}) + \text{const.} \quad (1)$$

We refer to $p(\mathbf{y} | \mathbf{x})$ as the measurement likelihood, or simply *likelihood*, and we refer to $p(\mathbf{x})$ as the *prior*. In this work, the posterior is based on a forward model for interferometric data and a score-based prior.

2.2. Score-based priors

A score-based diffusion model is a deep generative model that learns to sample from an image distribution (Song et al. 2021b; Sohl-Dickstein et al. 2015; Ho et al. 2020). We refer to its generative image distribution as a *score-based prior* and denote it as p_θ , where θ are the learned parameters. Given training images from a target prior p_{data} , the diffusion model is trained so that $p_\theta \approx p_{\text{data}}$.

Many methods have been developed to solve inverse problems with a pre-trained diffusion model (Song et al. 2022; Chung et al. 2022b; Chung & Ye 2022; Choi et al. 2021; Chung et al. 2022a, 2023; Jalal et al. 2021; Graikos et al. 2022; Kwar et al. 2022; Adam et al. 2022; Song et al. 2023; Mardani et al. 2023; Dia et al. 2023). However, these methods typically produce a conditional distribution that does not correspond to an exact posterior. Since we instead prioritize posterior estimation, we turn to a more accurate approach that approximates the posterior through variational inference with a standalone score-based prior (Feng et al. 2023; Feng & Bouman 2023).

The crucial benefit of a score-based diffusion model is that it allows for computing image probabilities under p_θ (Song et al. 2021b). That is, given any image \mathbf{x} , we can compute $\log p_\theta(\mathbf{x})$ through an analytical, differentiable formula. To sample from a posterior whose prior is a score-based prior, we can use any posterior-sampling approach that requires the value or gradient of the posterior log-density.

While $\log p_\theta(\cdot)$ has been used for posterior sampling (Feng et al. 2023), the function is slow to compute and only feasible for images with at most 32×32 pixels. We therefore appeal to a recently-proposed *surrogate* score-based prior that is more computationally efficient (Feng & Bouman 2023). The surrogate score-based prior is based on the evidence lower bound $b_\theta(\cdot)$ of a score-based prior. Instead of evaluating $\log p_\theta(\mathbf{x})$, we evaluate $b_\theta(\mathbf{x}) \leq \log p_\theta(\mathbf{x})$ as the surrogate log-density. Please refer to Appendix B for details about score-based diffusion models, including the formulae for $\log p_\theta(\cdot)$ and $b_\theta(\cdot)$.

2.3. EHT measurements

The EHT performs very-long-baseline interferometry (VLBI) with a global array of radio telescopes. Each pair of telescopes i, j , known as a *baseline*, provides a Fourier measurement called a *visibility* v_{ij} (van Cittert 1934; Zernike 1938; Thompson et al. 2017). However, the baselines only sparsely sample the complex 2D Fourier plane, or (u, v) space. Moreover, the visibilities are affected by thermal noise, station-dependent gain errors, and station-dependent phase errors (Collaboration et al. 2019e).

To overcome station-dependent errors, we use robust data products known as closure quantities. A *closure phase* (Jennison 1958) is given by a triplet of telescopes i, j, k and computed as $\angle(v_{ij}v_{jk}v_{ki})$. A *log closure amplitude* (Twiss et al. 1960) is given by a combination of four telescopes i, j, k, ℓ and computed as $\log\left(\frac{|v_{ij}||v_{k\ell}|}{|v_{ik}||v_{j\ell}|}\right)$. We denote the set of all linearly independent observed closure phases as $\mathbf{y}_{\text{cp}} \in \mathbb{R}^{N_{\text{cp}}}$ and that of log closure amplitudes as $\mathbf{y}_{\text{logca}} \in \mathbb{R}^{N_{\text{logca}}}$. In the case of visibilities with a high signal-to-noise ratio (i.e., $\text{SNR} > 1$), closure phases and log closure amplitudes approximately experience mean-zero Gaussian thermal noise (Rogers et al. 1995; Blackburn et al. 2020; Broderick & Pesce 2020) with standard deviations $\sigma_{\text{cp}} \in \mathbb{R}^{N_{\text{cp}}}$ and $\sigma_{\text{logca}} \in \mathbb{R}^{N_{\text{logca}}}$, respectively. We assume the high-SNR setting. Conditioned on an image \mathbf{x} , the measurement distribution can be modeled as Gaussian with log-likelihoods

$$\log p(\mathbf{y}_{\text{cp}} | \mathbf{x}) = -\frac{1}{2\sigma_{\text{cp}}^2} \|\mathbf{f}_{\text{cp}}(\mathbf{x}) - \mathbf{y}_{\text{cp}}\|_2^2 \quad \text{and} \quad \log p(\mathbf{y}_{\text{logca}} | \mathbf{x}) = -\frac{1}{2\sigma_{\text{logca}}^2} \|\mathbf{f}_{\text{logca}}(\mathbf{x}) - \mathbf{y}_{\text{logca}}\|_2^2, \quad (2)$$

where \mathbf{f}_{cp} and $\mathbf{f}_{\text{logca}}$ are nonlinear forward models. We note that the Gaussian noise is not purely (statistically) independent, but it is approximately independent under high-SNR visibilities or can be made independent under a linear transformation (Blackburn et al. 2020; Broderick & Pesce 2020; Arras et al. 2022). Please refer to Appendix C for details about interferometric data products and their forward models.

It is possible to use the same imaging algorithm with visibility amplitudes instead of log closure amplitudes. Visibility amplitudes, which have been used for other imaging results (Collaboration et al. 2019b; Medeiros et al. 2023), are more constraining than closure amplitudes, but they require calibration according to assumptions such as station-dependent systematic noise. In this work, we focus on using log closure amplitudes in order to avoid tuning the calibration assumptions. The original M87* work includes reconstructions from both types of data products for reference (Collaboration et al. 2019b).

3. METHOD

Our goal is to sample from an image posterior given EHT measurements and a desired image prior. The prior is obtained by training a score-based prior p_θ on images from the desired prior. The measurement likelihood is based on

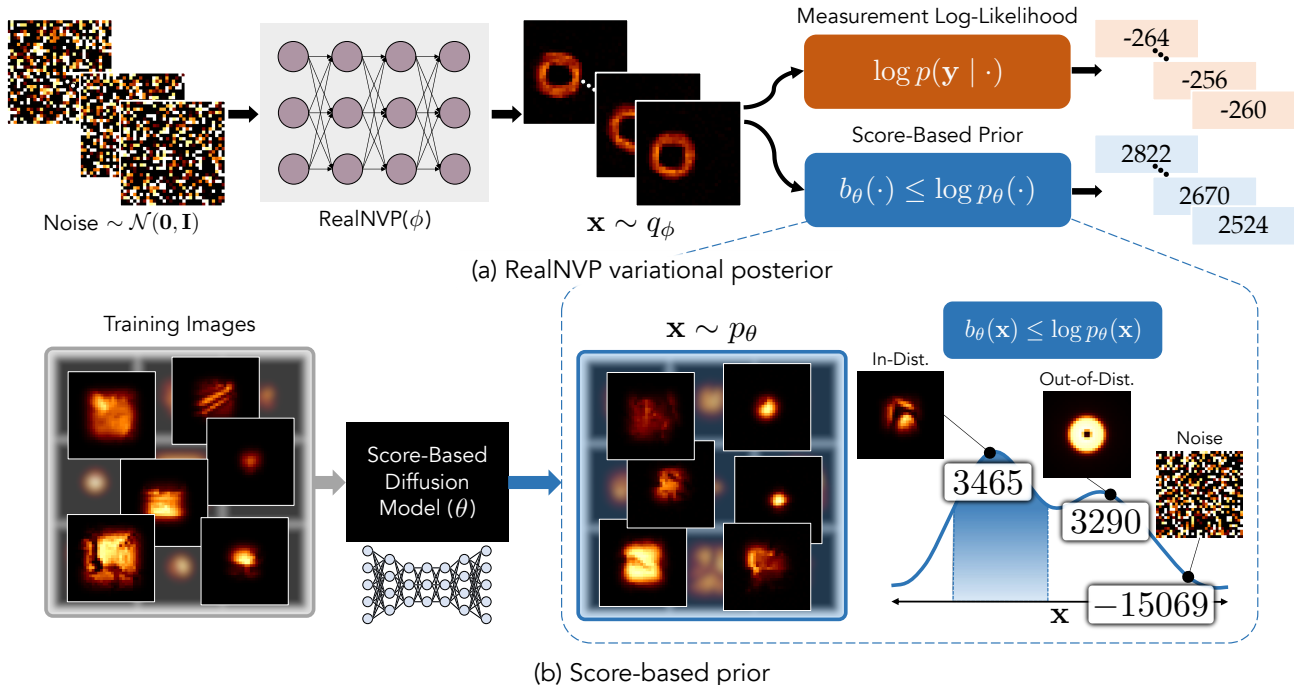


Figure 1. Method illustration. The CIFAR-10 prior was used for these examples; images are shown as 32×32 pixels on a $[0, 1]$ scale. At a high level, we optimize a variational distribution q_ϕ to approximate the image posterior $p_\theta(\cdot | \mathbf{y})$ given a score-based prior p_θ and log-likelihood based on EHT measurements. (a) illustrates our particular variational distribution: a RealNVP with parameters ϕ . At each optimization iteration i , the measurement log-likelihood (Eq. 2) and the log-density under the score-based prior of each sample \mathbf{x} from $q_\phi = q_{\phi^{(i)}}$ are evaluated. The average gradient is computed with respect to ϕ to update $\phi^{(i)}$. In other words, q_ϕ is optimized to produce samples that have high probability under both measurement likelihood and prior. (b) zooms into the score-based prior. A score-based prior is based on a score-based diffusion model, a deep generative model with parameters θ , that is trained on images from a target prior. Once trained, the diffusion model generates samples from a generative image distribution p_θ . There is an analytical formula for computing the evidence lower bound $b_\theta(\mathbf{x})$ of the log-probability $\log p_\theta(\mathbf{x})$ for any image \mathbf{x} , even for out-of-distribution images and images of pure noise.

a nonlinear forward model and Gaussian noise of closure quantities (Eq. 2). Thus the posterior log-density is given by

$$\begin{aligned} \log p_\theta(\mathbf{x} | \mathbf{y}) &= \log p(\mathbf{y} | \mathbf{x}) + \log p(\mathbf{x}) + \text{const.} \\ &= \log p(\mathbf{y}_{\text{cp}} | \mathbf{x}) + \log p(\mathbf{y}_{\text{logca}} | \mathbf{x}) + \log p_\theta(\mathbf{x}) - (V(\mathbf{x}) - \bar{V})^2 + \text{const.}, \end{aligned} \quad (3)$$

where $p_\theta(\mathbf{x} | \mathbf{y})$ is given a θ subscript to clarify its dependence on the score-based prior p_θ . We have introduced a flux-constraint objective $-(V(\mathbf{x}) - \bar{V})^2$, where $V(\mathbf{x})$ is the total flux (i.e., the sum of the pixel values) of the image \mathbf{x} and \bar{V} is the target total flux, because closure quantities do not constrain the total flux. We set \bar{V} as the median total flux of images sampled from the score-based prior p_θ and then scale posterior images to the original total flux as measured in the zero-baseline visibility. Please see Appendix A for a discussion on the flux-constraint objective. Note that since our priors were trained on compact centered images, we do not need an explicit center-of-light constraint.

Given this log-density equation (Eq. 3), we use variational inference (VI) (Zhang et al. 2018) to sample from $p_\theta(\mathbf{x} | \mathbf{y})$. VI approximates a complicated posterior with a tractable approximate distribution known as the variational distribution. Following the approach of Deep Probabilistic Imaging (DPI) (Sun & Bouman 2021), we use a RealNVP (Dinh et al. 2016) (a type of deep generative model known as a *normalizing flow* (Papamakarios et al. 2021)) with parameters ϕ as the variational distribution. Samples from the RealNVP are images \mathbf{x} from a distribution q_ϕ , and we

optimize ϕ to minimize the following KL divergence:

$$D_{\text{KL}}(q_\phi \| p(\cdot | \mathbf{y})) = \mathbb{E}_{\mathbf{x} \sim q_\phi} [-\log p(\mathbf{x} | \mathbf{y}) + \log q_\phi(\mathbf{x})] + \text{const.} \quad (4)$$

$$= \mathbb{E}_{\mathbf{x} \sim q_\phi} \left[-\log p(\mathbf{y}_{\text{cp}} | \mathbf{x}) - \log p(\mathbf{y}_{\text{logca}} | \mathbf{x}) - \log p_\theta(\mathbf{x}) + (V(\mathbf{x}) - \bar{V})^2 + \log q_\phi(\mathbf{x}) \right] + \text{const.} \quad (5)$$

$$\leq \mathbb{E}_{\mathbf{x} \sim q_\phi} \left[-\log p(\mathbf{y}_{\text{cp}} | \mathbf{x}) - \log p(\mathbf{y}_{\text{logca}} | \mathbf{x}) - b_\theta(\mathbf{x}) + (V(\mathbf{x}) - \bar{V})^2 + \log q_\phi(\mathbf{x}) \right] + \text{const.}, \quad (6)$$

where $b_\theta(\mathbf{x}) \leq \log p_\theta(\mathbf{x})$ is the log-probability of \mathbf{x} under the surrogate score-based prior (Feng & Bouman 2023), which is much more efficient than the exact $\log p_\theta(\mathbf{x})$. $\log q_\phi(\mathbf{x})$, a term that mathematically arises from the KL objective, is the log-probability under the variational distribution and can be interpreted as an entropy objective preventing mode collapse.

Our optimization problem is to minimize Eq. 6 with respect to the RealNVP parameters ϕ :

$$\phi^* = \arg \min_{\phi} \mathbb{E}_{\mathbf{x} \sim q_\phi} \left[-\log p(\mathbf{y}_{\text{cp}} | \mathbf{x}) - \log p(\mathbf{y}_{\text{logca}} | \mathbf{x}) - b_\theta(\mathbf{x}) + (V(\mathbf{x}) - \bar{V})^2 + \log q_\phi(\mathbf{x}) \right]. \quad (7)$$

We solve Eq. 7 with stochastic gradient descent, iteratively Monte-Carlo approximating the KL upper bound (Eq. 6) with a batch of samples from q_ϕ and computing the gradient with respect to ϕ . We find that annealing the weight of the data-fit terms gradually from 0 to 1 helps prevent bad local minima (see A.2 for a discussion on data annealing). Once ϕ is optimized, samples $\mathbf{x} \sim q_\phi$ can be efficiently obtained as samples from an approximate posterior. The RealNVP occasionally outputs slightly negative pixel values, so we clip samples at inference time to a minimum value of 0 to impose a positivity constraint. Please refer to Appendix E for implementation details. Fig. 1 illustrates the essential components of our imaging method: the RealNVP variational posterior and the score-based prior.

3.1. Score-based priors used in this work

In this work, we focus on the following score-based priors, each trained on a dataset of images assuming a 128- μas field of view (FOV). Unless stated otherwise, we use the terms ‘‘prior’’ and ‘‘score-based prior’’ synonymously. Fig. 2 shows samples from each prior.

- The **CIFAR-10** prior was trained on the CIFAR-10 (Krizhevsky & Hinton 2009) dataset of 32×32 images from ten object classes (e.g., airplane, automobile, dog). We used a training set of 45k grayscale images. The images were tapered on the edges to incorporate assumptions of a black background and a centered object. A tapering effect is created by defining a binary mask with a center square region of pixels set to 1 and everywhere else set to 0, then applying a Gaussian blur kernel with standard deviation 8 μas , and then element-wise multiplying the blurred mask with the image. The size of the taper was randomly varied during training by randomly varying the size of the center square region of the mask, resulting in a centered compact region of between 12.8×12.8 and $83.2 \times 83.2 \mu\text{as}$.
- The **GRMHD** prior was trained on 100k images from GRMHD simulations (Wong et al. 2022) of SgrA* resized to 64×64 pixels. During training, the GRMHD images were randomly zoomed between -16.7% (zoomed-in) and $+14.5\%$ (zoomed-out), thus varying the diameter of the thin ring to be between 35 and 48 μas .
- The **RIAF** prior was trained on 9070 images of RIAF (Broderick et al. 2011) simulations. The RIAF images were downloaded¹ with all available spin and inclination parameters and resized to 32×32 . During training, they were also randomly zoomed between -16.7% and $+14.5\%$, and they were randomly rotated between -2π and $+2\pi$.
- The **CelebA** prior was trained on the CelebA (Liu et al. 2015) dataset of celebrity faces. We used a training set of 160k images that were resized to 32×32 . The same tapering effect that was used for CIFAR-10 was applied. Although far from a reasonable prior for astronomical images, a prior trained on faces helps us see what happens when strong but probably incorrect assumptions are made.

¹ <http://vlbiimaging.csail.mit.edu/myData>

The RIAF and GRMHD priors incorporate strong assumptions about a ring structure. The CIFAR-10 and CelebA priors, on the other hand, do not assume any ring structure or even the presence of an astronomical object. One might make the following order of priors from weak to strong assumptions: CIFAR-10, GRMHD, RIAF. In addition, we have the CelebA prior, which makes specific assumptions against our expectations.

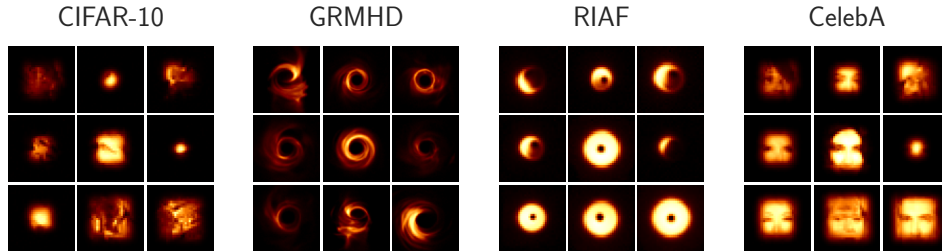


Figure 2. Score-based priors used in this work. Nine samples from each learned prior are shown.

4. M87* RESULTS

We estimated image posteriors of M87* given the EHT observations from April 2017. For each of the four observation days, we gathered the closure phases and log closure amplitudes from the combined low-band and high-band public data.² We used the same preprocessing steps as the eht-imaging algorithm used in the original M87* imaging work (Collaboration et al. 2019b) (assuming non-closing fractional systematic noise of 0.03), except we did not add station-dependent systematic noise since we do not need to calibrate the visibility amplitudes. Fig. 3 shows image reconstructions of M87* under the four score-based priors. Although imaging was done with a prior-dependent total flux and either 32×32 or 64×64 pixels depending on the prior, we re-scale images to have a total flux of 0.6 Jy and resize them to 128×128 for visualization.

The CIFAR-10 and CelebA priors, which incorporate no assumptions about black holes, lead to images with a ring-like structure. The CelebA reconstructions include some face-like details, especially for April 10, the day with the fewest observations and thus the day whose image is least constrained by measurements. Nonetheless, the fact that both the black-hole-agnostic priors recover ring shapes is strong evidence of a ring-like structure in the measurements. It also reveals that basic natural-image statistics shared by CIFAR-10 and CelebA may be sufficient to retrieve the ring structure under a constrained FOV.

The GRMHD and RIAF priors lead to images with a well-defined ring structure. The GRMHD prior is visually richer, encouraging a thin ring with wispy features in the bright region of the ring. The RIAF prior constrains the image according to a simplified geometric model without adding any lower-level details.

Tab. 1 confirms that all the reconstructed images are consistent with the EHT measurements. The table reports the reduced χ^2 — we note that it is not a true reduced χ^2 since we only incorporate image pixels as degrees of freedom, but it is useful as a proxy metric of data consistency. Across priors and observation days, the χ^2 values are < 1.5 , which is considered a good sign of fitting the measured data. The RIAF prior struggles most to fit the data (most of its χ^2 values are greater than 1) because it imposes the most constraining black-hole model. The rest of the priors tend to result in $\chi^2 < 1$, which means that they are flexible enough to somewhat over-fit the data and that any differences between their posteriors are likely due to the visual biases of the priors that are not constrained by the data.

4.1. Characterizing the posteriors

In addition to evaluating single samples from the posterior (Fig. 3), we can assess aspects of the posterior distribution such as multimodality and uncertainty. Our imaging approach leads to single-mode M87* image posteriors, except for some CelebA posteriors that are bimodal (Fig. 5). We note that the number of modes in the estimated posterior may be due to the variational family being used; in the future, a more expressive family of distributions parameterized through a better network architecture may identify more modes.

² https://datacommons.cyverse.org/browse/iplant/home/shared/commons_repo/curated/EHTC_FirstM87Results_Apr2019

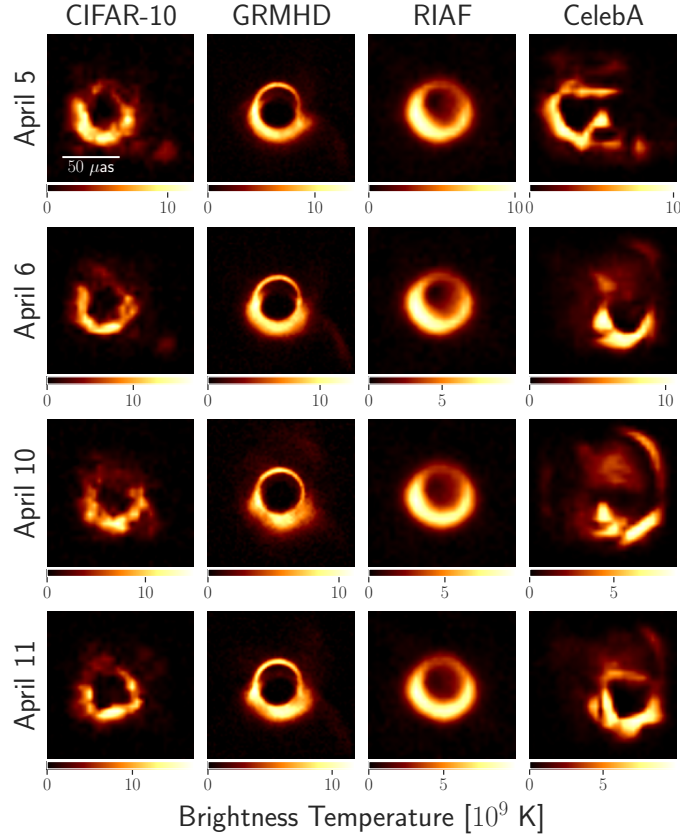


Figure 3. M87* posterior samples. A random posterior image is shown for each observation day and prior. The CIFAR-10 prior was trained on images of everyday objects and makes no assumptions of black-hole structure, yet it recovers a ring-like structure for all four observation days. The GRMHD prior assumes a fluid-flow model of black holes, which helps it recover visually-striking images of a thin ring with wisps. The RIAF prior assumes a simplified crescent model of black holes, which results in simplified crescent images of M87*. The CelebA prior was trained on images of human faces, so its preferred images are presumably far away from the true source image. Even with its incorrect and strong biases, the CelebA prior recovers a ring-like structure, here favoring an eye from the face prior to explain the ring. These images under various priors all fit the EHT observations but incorporate different visual biases.

Fig. 4 shows Gaussian fits of the posteriors estimated under the CIFAR-10, GRMHD, and RIAF priors. Under all these priors, the mean image shows a clear progression of the bright spot of the ring moving counter-clockwise over the four observation days. The pixel-wise standard deviation shows areas of uncertainty around the mean. The results in Fig. 4 show that as the prior becomes stronger (i.e., from CIFAR-10 to GRMHD to RIAF), the uncertainty goes down. Under the CIFAR-10 and GRMHD priors, there is uncertainty throughout the ring, whereas under the RIAF prior, uncertainty lies mainly along the edges of the ring.

Fig. 5 visualizes the bimodal posteriors under the CelebA prior. Like with CIFAR-10, the magnitude of the uncertainty is higher than that of the GRMHD and RIAF priors. The presence of multiple modes further reflects higher uncertainty under the CelebA prior, which makes sense for a prior that is so mismatched to the observed data.

A feature that stands out in the CIFAR-10, GRMHD, and CelebA reconstructions is a southwest region of extended flux outside the ring. It is especially noticeable in the April 5 and 6 images. See, for example, the faint spot of brightness in the CIFAR-10 reconstructions and the faint wisp to the southwest in the GRMHD reconstructions in Figs. 3 and 4. A disconnected southwest region of brightness also appears in both modes of the CelebA posterior on April 5 and in the second mode of the April 6 posterior in Fig. 5. Such a feature is not visible in the RIAF reconstructions. With previous imaging results that only incorporated one prior, it would have been difficult to conclude whether this feature were an artifact of imaging or a clue from the data. Our results in Figs. 4 and 5 suggest that it is a prior-dependent feature, with different priors placing different amounts of brightness in that southwest region.

		CIFAR-10	GRMHD	RIAF	CelebA
April 5	χ_{cp}^2	0.80 ± 0.03	0.83 ± 0.15	1.16 ± 0.07	0.80 ± 0.03
	χ_{logca}^2	0.75 ± 0.04	0.76 ± 0.09	1.42 ± 0.11	0.71 ± 0.04
April 6	χ_{cp}^2	0.92 ± 0.02	0.93 ± 0.05	1.05 ± 0.03	0.93 ± 0.03
	χ_{logca}^2	0.76 ± 0.02	0.74 ± 0.04	0.96 ± 0.04	0.80 ± 0.06
April 10	χ_{cp}^2	0.92 ± 0.05	0.89 ± 0.04	1.34 ± 0.08	0.90 ± 0.05
	χ_{logca}^2	0.73 ± 0.06	0.71 ± 0.04	1.29 ± 0.12	0.72 ± 0.06
April 11	χ_{cp}^2	1.09 ± 0.02	1.06 ± 0.02	1.25 ± 0.04	1.08 ± 0.03
	χ_{logca}^2	0.69 ± 0.04	0.65 ± 0.04	0.97 ± 0.06	0.65 ± 0.03

Table 1. Data-consistency metrics (χ^2) for closure quantities of M87* data. χ_{cp} and χ_{logca} are the χ^2 metrics for closure phases and log closure amplitudes, respectively. The avg. \pm std. dev. of 128 samples from the estimated posterior is reported. $\chi^2 \approx 1$ indicates a good balance between fitting the observed data and fitting the prior. Lower χ^2 means more data consistency. The RIAF prior leads to the highest χ^2 values, meaning the strength of this prior relative to the data is strongest. This is probably because the RIAF model is the most constraining of the priors.

To summarize our findings from the estimated M87* posteriors, the most notable result is that all priors recover ring-like structure. The priors that do not assume a black hole (i.e., CIFAR-10 and CelebA) exhibit most uncertainty in the posterior and are most flexible with adding flux outside of the ring. The priors based on a black-hole model (i.e., GRMHD and RIAF) reconstruct the clearest rings, with the GRMHD prior providing the most visual detail. In general, the more constraining the prior, the less uncertainty there is in the posterior, but the more potential there is to overfit to prior assumptions.

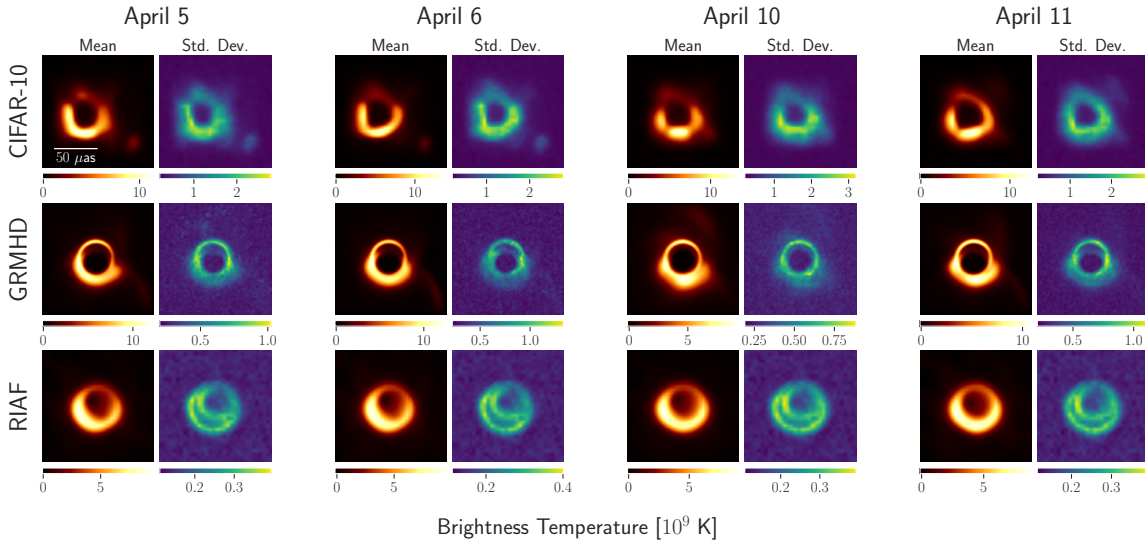


Figure 4. Mean and std. dev. of posterior samples. Uncertainty decreases as the prior becomes stronger (i.e., maximum std. dev. decreases from CIFAR-10 to GRMHD to RIAF). Note that under the CIFAR-10 prior, the day with the most uncertainty is April 10, the day with the least data. The stronger priors (i.e., GRMHD and RIAF) do not exhibit more uncertainty for this day compared to other days.

5. SIMULATED-DATA RESULTS

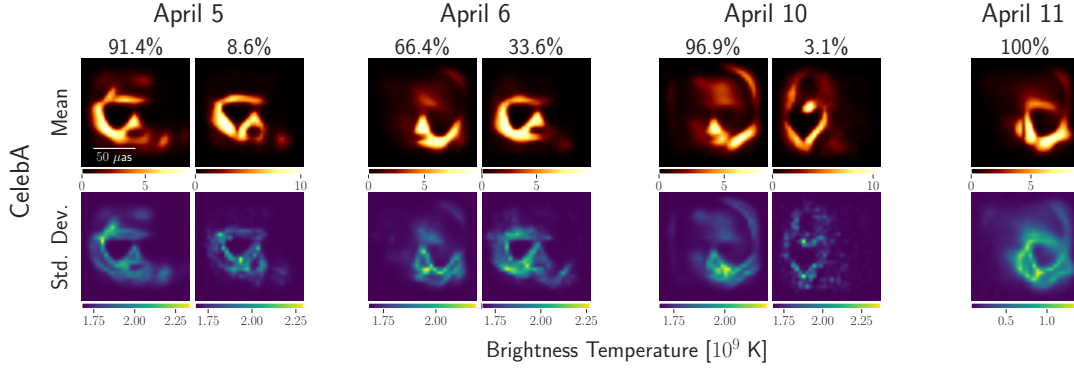


Figure 5. Bimodal M87* image posteriors under the CelebA prior. A two-component Gaussian-mixture model was fit to 128 posterior samples for April 5, 6, and 10. The mean, std. dev., and weight of each Gaussian-mixture component are shown. The only single-mode posterior is for April 11, which is the day with the most (u, v) coverage.

We validate our imaging approach on simulated observations of synthetic source images. A crucial advantage of our approach is that it does not involve parameter-tuning. As we do not need to hand-tune hyperparameters based on a calibration dataset, the experiments presented in this section are simply meant to verify the efficacy of the approach.

Fig. 6 shows results for a dataset of eight source images. Among the images are validation images used in the original M87* imaging work (Collaboration et al. 2019b) and two images of an elliptical object used in the SgrA* imaging work (Collaboration et al. 2022). All observations were simulated based on the April 6 observing array.

The quality of image reconstruction heavily depends on the prior. For example, the GRMHD reconstruction of GRMHD 1 appears more convincing than the GRMHD reconstruction of the Double image in Fig. 6. On the other hand, the RML methods used in previous EHT imaging efforts (Collaboration et al. 2019b, 2022) achieve overall cleaner reconstructions of synthetic data. One reason for the better performance of those RML methods is that they use regularization parameters chosen based on a calibration dataset that is very similar to their test images. In contrast, we consider priors that may be profoundly different from the true source image (e.g., CelebA prior applied to the Double data). Another reason is that RML methods produce a mean image that tends to be cleaner than individual posterior samples, which are shown in Fig. 6. We emphasize that the goal of our work is not to achieve the cleanest or most accurate reconstructions. Rather, we aim to showcase the effects of different priors, even when those priors might not lead to the best reconstruction due to mismatch with the data.

Overall, the reconstructed images make sense according to the biases of the prior. The CelebA prior introduces face-like features, especially when the ground-truth source object is fairly “flat” (e.g., the Disk and Elliptical images). As was the case with M87*, the CelebA prior is the only one that leads to multimodal estimated posteriors. Images under the RIAF prior are always centered and ring- or disk-like. The GRMHD prior always prefers the presence of a thin ring at the center of the image. The CIFAR-10 prior imposes weak biases and appears to assemble images from small locally-smooth patches.

Tab. 2 quantifies the performance of the various priors on each source image. As in previous work (Collaboration et al. 2019b, 2022), we evaluate the normalized cross-correlation (NCC). Since our approach does not explicitly constrain the center-of-light, we use a shift-invariant NCC metric, which is computed as the maximum NCC between all shifted versions of the reconstructed image and the ground-truth image. As expected, the closer the prior is to the ground-truth image, the more accurately it recovers the ground-truth image. For example, the GRMHD prior excels at recovering the Ring, Crescent, and GRMHD images but struggles with the non-ring-like images. The RIAF prior performs well on ring-like images and disk-like images. The CelebA prior, unsurprisingly, performs poorly on this dataset of images. The CIFAR-10 prior does best compared to the other priors at recovering the non-ring-like images (e.g., Double and Point+Elliptical). It performs generally well across all the source images, suggesting that it serves as an effective “general-purpose” prior.

We report χ^2 metrics for these simulated data in Tab. 3. There does not appear to be a correlation between the χ^2 statistics in Tab. 3 and the NCC statistics in Tab. 2. The results in Tab. 3 simply confirm data consistency of the reconstructed images, as χ^2 values are consistently less than 2 and often close to 1 (lower χ^2 corresponds to more data consistency, and $\chi^2 \approx 1$ is considered a sign of a good balance between data and prior). As was the case with M87*, the RIAF prior results in the highest χ^2 values, perhaps because it is the most constraining prior. Overall, our tests

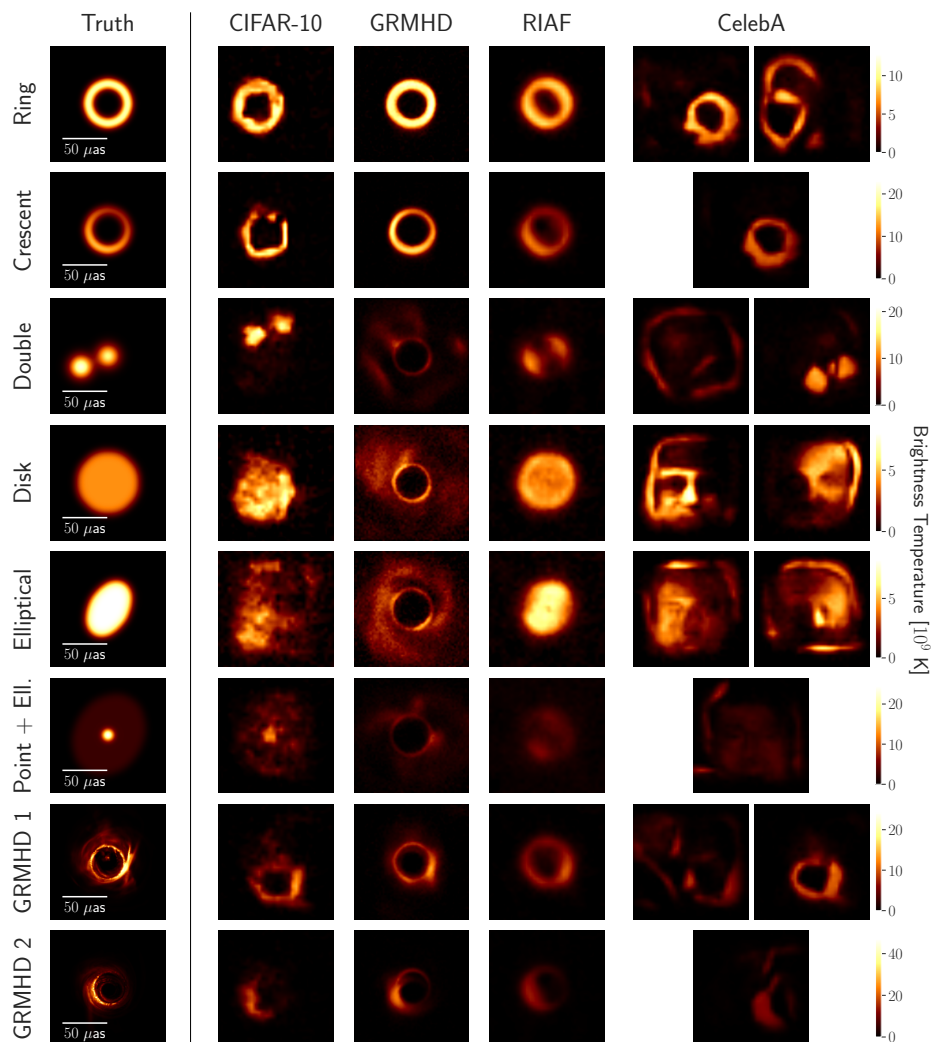


Figure 6. Image reconstructions from simulated data. A sample (one sample from each mode if the posterior is bimodal) is shown from each estimated posterior. Qualitatively, the CIFAR-10 prior adds the least amount of bias, producing reasonable reconstructions of each image in this dataset. The GRMHD prior strongly prefers a centered ring in the image. The RIAF prior prefers a centered ring- or disk-like structure in the image. The CelebA prior struggles to recover these source images, in some cases adding face features. However, it performs decently well on certain images like the Crescent and GRMHD images. As with the M87* reconstructions, the CelebA prior leads to the most multimodal posteriors. When the source image is known to be well-approximated by a GRMHD or RIAF model, the more constrained GRMHD or RIAF prior may be the best choice.

on simulated data confirm that the score-based priors impose the expected biases on the image reconstruction while allowing for reasonable data consistency.

5.1. Characterizing the simulated-data posteriors

Fig. 7 shows the mean and uncertainty of posteriors under the CIFAR-10, GRMHD, and RIAF priors. It conveys a similar finding as that of the M87* posteriors (Fig. 4) that uncertainty decreases as the prior becomes stronger. For a weak prior like CIFAR-10, which leads to high posterior uncertainty, it can be helpful to consider the mean reconstruction instead of noisier individual samples.

	CIFAR-10	GRMHD	RIAF	CelebA
Ring	0.95 ± 0.009	0.98 ± 0.024	0.95 ± 0.003	0.88 ± 0.090
Crescent	0.85 ± 0.019	0.96 ± 0.007	0.92 ± 0.005	0.95 ± 0.007
Double	0.94 ± 0.009	0.49 ± 0.028	0.93 ± 0.004	0.39 ± 0.130
Disk	0.95 ± 0.007	0.59 ± 0.027	0.98 ± 0.002	0.80 ± 0.020
Elliptical	0.79 ± 0.037	0.50 ± 0.029	0.97 ± 0.003	0.75 ± 0.026
Point + Ell.	0.87 ± 0.022	0.58 ± 0.031	0.73 ± 0.011	0.43 ± 0.026
GRMHD 1	0.84 ± 0.015	0.86 ± 0.009	0.84 ± 0.004	0.46 ± 0.089
GRMHD 2	0.85 ± 0.012	0.90 ± 0.003	0.85 ± 0.004	0.77 ± 0.012

Table 2. Normalized cross-correlation (NCC). The avg. \pm std. dev. of the NCC metric for 128 samples from the posterior is reported (highest NCC in each row is bolded). In general, the closer the prior is to the ground-truth image, the closer its posterior samples are to the ground-truth. For example, the Ring, Crescent, and GRMHD images are best reconstructed with the GRMHD prior, whereas non-ring-like images are poorly reconstructed with the GRMHD prior. The CIFAR-10 prior may be the best “general-purpose” prior, giving NCC values between about 0.80 and 0.95 across these images.

		CIFAR-10	GRMHD	RIAF	CelebA
Ring	χ_{cp}^2	0.87 ± 0.02	0.90 ± 0.03	0.93 ± 0.02	0.89 ± 0.04
	χ_{logca}^2	0.72 ± 0.03	0.75 ± 0.05	1.06 ± 0.06	0.72 ± 0.03
Crescent	χ_{cp}^2	0.73 ± 0.02	0.76 ± 0.02	0.82 ± 0.03	0.73 ± 0.02
	χ_{logca}^2	0.67 ± 0.02	0.78 ± 0.03	0.96 ± 0.06	0.68 ± 0.02
Double	χ_{cp}^2	0.96 ± 0.02	1.00 ± 0.03	1.00 ± 0.03	0.99 ± 0.03
	χ_{logca}^2	0.77 ± 0.02	0.81 ± 0.04	1.21 ± 0.07	0.84 ± 0.03
Disk	χ_{cp}^2	1.82 ± 0.04	1.83 ± 0.05	1.81 ± 0.03	1.81 ± 0.05
	χ_{logca}^2	1.30 ± 0.04	1.56 ± 0.14	1.45 ± 0.05	1.42 ± 0.06
Elliptical	χ_{cp}^2	1.76 ± 0.04	1.76 ± 0.04	1.88 ± 0.04	1.79 ± 0.04
	χ_{logca}^2	1.44 ± 0.03	1.64 ± 0.06	1.66 ± 0.05	1.43 ± 0.03
Point + Ell.	χ_{cp}^2	1.22 ± 0.02	1.21 ± 0.02	1.36 ± 0.04	1.24 ± 0.02
	χ_{logca}^2	0.83 ± 0.02	0.83 ± 0.03	1.04 ± 0.05	0.84 ± 0.02
GRMHD 1	χ_{cp}^2	0.90 ± 0.02	0.89 ± 0.07	1.00 ± 0.04	0.90 ± 0.05
	χ_{logca}^2	0.72 ± 0.03	0.70 ± 0.03	1.05 ± 0.07	0.83 ± 0.03
GRMHD 2	χ_{cp}^2	0.59 ± 0.02	0.59 ± 0.01	0.63 ± 0.03	0.60 ± 0.02
	χ_{logca}^2	0.51 ± 0.02	0.56 ± 0.03	1.00 ± 0.08	0.53 ± 0.02

Table 3. Data-consistency metrics (χ^2) for closure quantities of simulated data. χ_{cp} and χ_{logca} are the χ^2 metrics for closure phases and log closure amplitudes, respectively. The avg. \pm std. dev. of 128 samples from the estimated posterior is reported. Lower χ^2 is a sign of higher data consistency. $\chi^2 \approx 1$ is considered an indication of a good balance between the observed data and the prior. The Disk, Elliptical, and Point+Elliptical images are the most challenging cases for these particular priors, as evidenced by the high χ^2 values that indicate data-fitting difficulty.

Fig. 8 characterizes some of the bimodal posteriors recovered by the CelebA prior. It is perhaps reassuring that a prior with such erroneous assumptions (i.e., that face statistics well describe these particular source images) is able to account for mismatches with the data through a wider posterior. For example, for the Ring, Double, and GRMHD 1 data, the posterior covers two modes, one of which accurately recovers the ground-truth image.

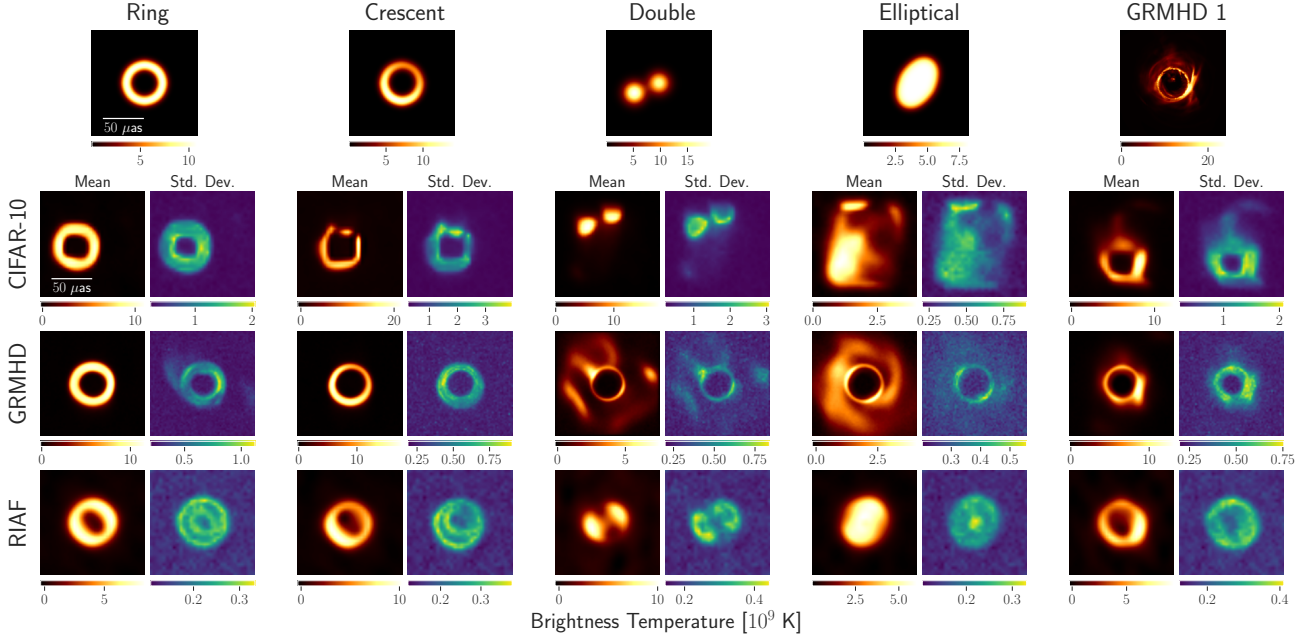


Figure 7. Mean and std. dev. of simulated-data posteriors. As in Fig. 4 with M87* data, we find with simulated data that uncertainty decreases with a stronger prior. CIFAR-10 exhibits the most uncertainty (i.e., highest std. dev.) given that it is the most flexible of the priors. Compared to the individual samples in Fig. 6, the mean images appear much cleaner.

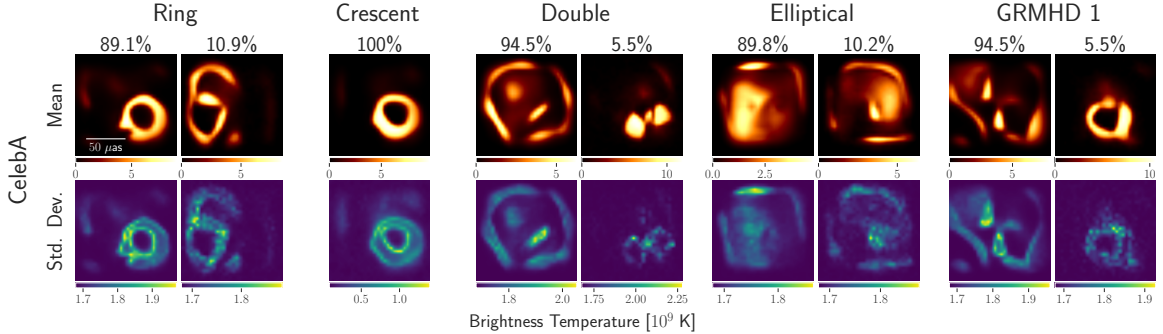
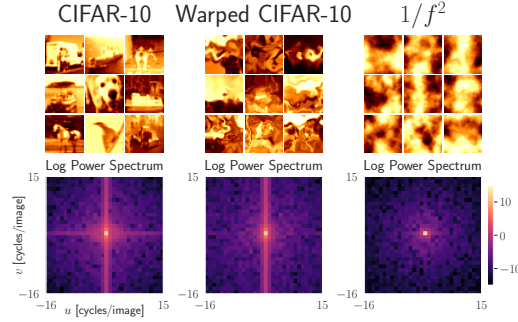


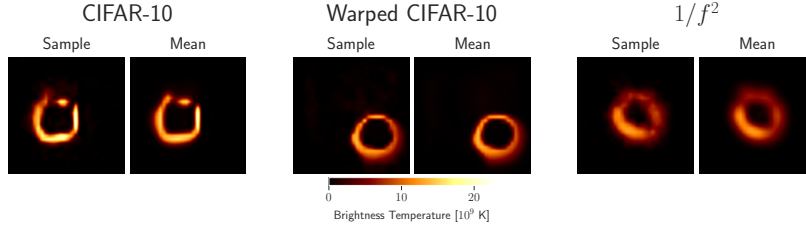
Figure 8. Mean and std. dev. of simulated-data posteriors under the CelebA prior. Like with the M87* data (Fig. 5), the CelebA prior is the only one that gives rise to bimodal posteriors. For each posterior, a one- or two-component Gaussian-mixture model (one for a single-mode posterior and two for a bimodal posterior) was fit to 128 samples. The mean, std. dev., and weight of each Gaussian component are shown. For the Ring, Double, and GRMHD 1 data, one of the two modes is quite similar to the ground-truth image while the other is not.

5.2. Biases of the CIFAR-10 prior

While CIFAR-10 represents a “generic” natural-image prior, the dataset itself still contains biases. The CIFAR-10 dataset comprises upright images of animals and man-made objects, which tend to exhibit horizontal or vertical lines. As Fig. 5.2 shows, the average log power spectrum of CIFAR-10 images has most power in the purely horizontal or vertical spatial frequencies. This preference for vertically- or horizontally-oriented edges results in images of objects



(a) Image statistics of CIFAR-10 and alternative natural-image datasets



(b) Crescent reconstructions under alternative natural-image priors

Figure 9. Reducing the CIFAR-10 bias toward horizontal lines and vertical lines. For example, given simulated data of the Crescent image from Fig. 6, this bias results in posterior images containing a boxy object, even though the actual Crescent is a ring without any straight edges. This is likely due to the statistics of the CIFAR-10 dataset, which contains mostly man-made objects and animals. Such images include many sharp corners and lines arising from boxy objects like cars, the legs of standing animals, or horizon lines. Although CIFAR-10 is our choice of a generic natural-image prior, it is possible to define an alternative natural-image prior with less preference for vertically- or horizontally-oriented edges. We tested a prior trained on CIFAR-10 images that underwent warped random affine transforms and a prior trained on 32×32 images with power spectral density proportional to $1/f^2$ (since the power spectra of natural images have been shown to follow a $1/f^\alpha$ trend, where f is the spatial frequency in cycles per image (van der Schaaf & van Hateren 1996), and α is typically between 1 and 3). The CIFAR-10, Warped CIFAR-10, and $1/f^2$ priors were all trained with the same number of training images (45k), with the same tapering effect described in Sec. 3.1, and for the same number of iterations (100k). (a) shows nine training samples and the average log power spectrum of 10k training samples (without the taper) for each prior. The average spectral power of CIFAR-10 images is relatively high in the horizontal and vertical frequencies. Warping the CIFAR-10 images seems to reduce the preference for vertical frequencies, but a large presence of horizontal frequencies remains (perhaps in part because horizons are still distinguishable after warping, as can be seen in some of the training samples). The $1/f^2$ noise images have isotropically-distributed spectral power. (b) shows results of imaging the Crescent simulated data under the different priors. A posterior sample and the average of 128 posterior samples are shown for each prior. With the regular CIFAR-10 prior, there is a sharp corner at the top-right of the ring-like object that makes it look squarish. This artifact is not present in the Warped CIFAR-10 reconstructions, which more resemble a smooth ring. The $1/f^2$ prior, which does not have a preference for any frequency orientation, also recovers an object that resembles a smooth ring.

that look somewhat rectangular instead of circular, even given measurements of a ring structure. See, for example, the CIFAR-10 reconstructions from the Crescent and GRMHD 1 data in Figs. 6 and 7 or the April 10 and 11 CIFAR-10 reconstructions of M87* in Fig. 4. In Fig. 9, we demonstrate on the Crescent data how boxy artifacts can be mitigated with a prior trained on warped CIFAR-10 images or a prior trained on images with a $1/f^2$ spectral distribution. By distorting CIFAR-10 images with warped random affine transforms, we expect to reduce the presence of straight lines by perturbing them to have more curvature. Alternatively, by randomly sampling from a $1/f^2$ spectral distribution, we create a dataset of images that follow a simplified statistical model without any preference for straight lines.

6. EXTRACTED RING FEATURES

An important stage of analysis is to extract ring features from reconstructed images, distilling any ring structure into a few parameters dictating its geometry and brightness profile. In Collaboration et al. (2019c) and Collaboration

et al. (2019c), the EHT Collaboration extracted, among other quantities, the following characteristic ring features: diameter, width, orientation, asymmetry, and fractional central brightness. It found the ring diameter and orientation angle to be most consistent across imaging methods, with the other quantities varying depending on the imaging pipeline. In this paper, we focus on these characteristic features and analyze the effect of the prior on them.

The **diameter** d indicates the full size of the ring and is calculated based on the distance between the peak brightness and the ring center. The **width** w indicates the thickness of the ring itself. The **orientation** angle n , measured east of north, roughly indicates the radial position of most of the brightness. The azimuthal **asymmetry** A , a measure of brightness asymmetry throughout the ring, roughly indicates the magnitude of brightness at the measured orientation. The **fractional central brightness** f_C indicates how bright the interior of the ring is compared to the ring itself and can be considered an inverse brightness contrast ratio. We use the REx feature extraction algorithm (Chael 2019) implemented in the `eht-imaging` library. d and f_C are measured the same way as in Collaboration et al. (2019b), but the other features have slight differences (we default to following the REx implementation rather than the equations provided in Collaboration et al. (2019b)). Appendix D contains the exact equations we used to compute these features. Fig. 11 helps visualize some of the features.

6.1. Ring features of simulated-data reconstructions

We performed feature extraction on images from simulated data, focusing on the source images with ring-like structure: Crescent, Ring, GRMHD 1, and GRMHD 2. We analyzed the recovered posteriors under all the score-based priors but excluded the non-ring-like samples from the CelebA posteriors for the Ring and GRMHD 1 data (see Fig. 6, which shows that the second mode of the Ring posterior and the first mode of the GRMHD 1 posterior do not have a ring-like structure). Fig. 10 shows all the extracted features and their error bars. In the following paragraphs, we discuss each feature and its dependence (or lack thereof) on the prior.

Diameter. All priors recover the diameter of the source image (within one standard deviation from the mean extracted diameter). The only exception is that the RIAF prior leads to a larger diameter for GRMHD 1. A possible explanation is that the RIAF model is too strong of a prior for this data, as it must account for all the flux in the image with a thick crescent (as evidenced by the relatively high extracted diameter and width of the RIAF-reconstructed images). The RIAF prior also leads to the highest χ^2 values (Tab. 3), further evidence that it has difficulty fitting the GRMHD 1 observations. On the other hand, the RIAF prior correctly recovers the diameter and has lower χ^2 values for the Ring and Crescent, two objects that can be well-approximated with a RIAF model. Even though the diameter should be well-constrained by the measurements, our results demonstrate how a strong-enough prior may recover a ring structure but with an incorrect diameter.

The CIFAR-10 prior gives the most accurate mean diameter, although with greater uncertainty than the GRMHD and RIAF priors. This makes sense as the CIFAR-10 prior, in making the weakest assumptions, is most flexible with the image reconstruction. The CelebA prior exhibits significantly high uncertainty for GRMHD 2, perhaps because its recovered images have the least ring-like structure (Fig. 6). The GRMHD prior accurately recovers the diameter across all these ring-like data and with relatively little uncertainty.

Width. The ring width varies significantly with the prior, which supports previous findings that the width is less well-constrained by the measurements than the diameter is (Collaboration et al. 2019b,c). The GRMHD prior recovers the thinnest rings as a result of being trained on GRMHD images that exhibit thin rings.

Orientation. All priors recover the orientation angle of the source image, except the CelebA prior given GRMHD 2 data. Like the high diameter uncertainty, this may be due to the reconstructed images having relatively weak ring structure. As can be seen in the two samples from this posterior in Fig. 6, there is actually some brightness outside of the ring-like area. These results further highlight that strong and incorrect assumptions in the prior may inhibit correct recovery of ring features that should be constrained by the observations. Besides this extreme case of applying a CelebA prior to GRMHD data, the ring orientation appears to be independent of the prior.

Asymmetry. The brightness asymmetry appears to be fairly robust to the prior. Again, the exception is the CelebA prior applied to the GRMHD 2 data, which can be explained by the weak ring structure present in the CelebA-recovered images. We note that for the Ring data, which has no asymmetry, all priors produce a slight asymmetry, which is unavoidable with most imaging algorithms (Collaboration et al. 2019b).

Fractional central brightness. This feature varies extremely with the prior, and the original M87* imaging work also found that f_C is not well-constrained by the data (Collaboration et al. 2019b). The GRMHD prior recovers the lowest fractional central brightness for the GRMHD observations. Along with smaller ring widths, these low f_C values

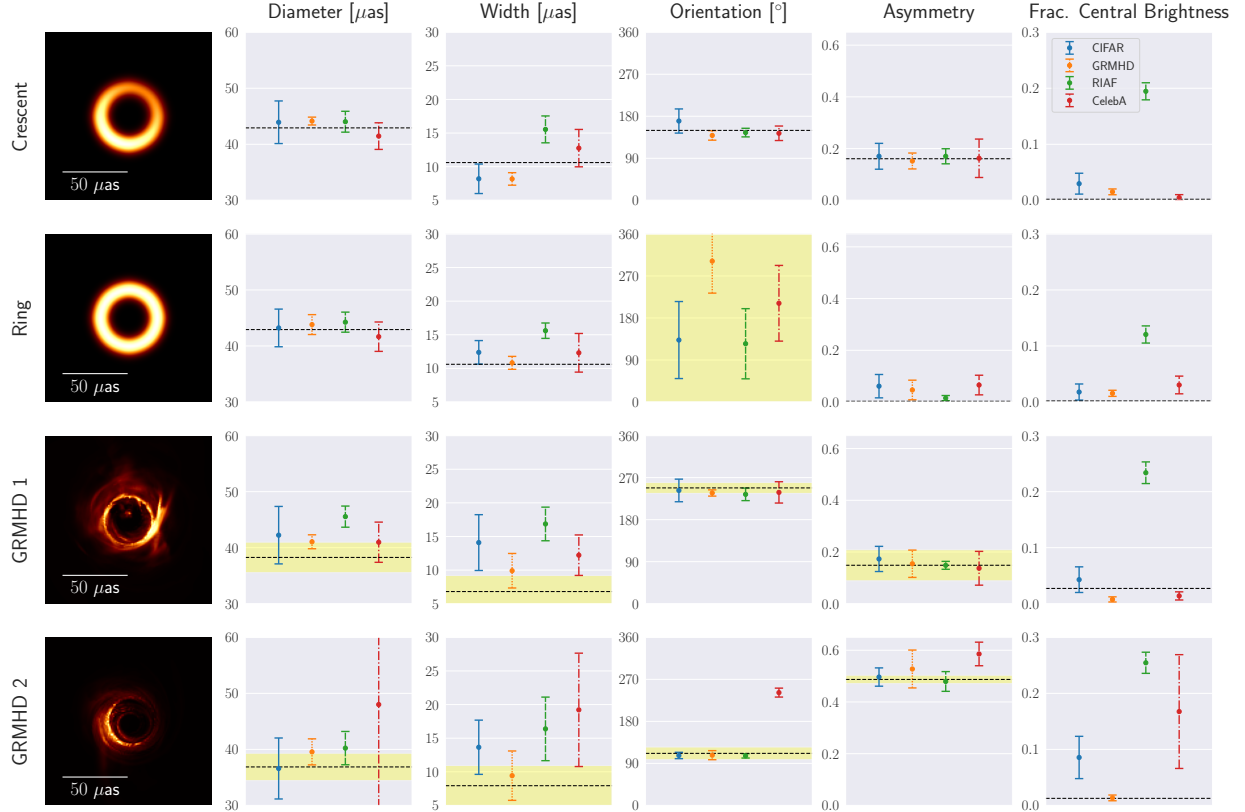


Figure 10. Extracted ring features of images reconstructed from simulated data. The dotted line indicates the measured quantity of the ground-truth image, and the shaded yellow region indicates the std. dev. as computed by REx (the orientation of the Ring image was manually set to span 0° to 360°). For the score-based priors (CIFAR, GRMHD, RIAF, CelebA), the mean was computed across the measured quantities of 128 posterior samples. The std. dev. for all features except fractional central brightness (f_C) was computed as the square root of the average variance across these samples. Since REx does not provide uncertainty for f_C of a single image, the f_C error bars were computed as the std. dev. of the f_C values of all posterior samples. All choices of prior roughly recover the target diameter, orientation, and asymmetry. The only exceptions are that the RIAF prior over-estimates the diameter of GRMHD 1 (due to the difficulty of fitting GRMHD data to a strong RIAF prior) and that the CelebA prior over-biases the orientation of GRMHD 2 (due to the CelebA prior struggling to produce a strong ring structure with such data). The width and fractional central brightness are particularly prior-dependent, with the GRMHD prior providing consistently small values for these features. In contrast, the RIAF prior prefers large widths and high f_C values. Please see Fig. 6 for image samples.

indicate that using a well-matched GRMHD prior on GRMHD observations gives the benefit of sharper images than could be obtained with a weaker prior like CIFAR-10.

6.1.1. Discussion

To summarize our results on simulated data, we find that the recovered ring diameter, orientation angle, and asymmetry are fairly robust to the image prior, while the width and fractional central brightness are tied to the prior. However, it is possible to overly bias the diameter with an overly-biased prior. In particular, the RIAF prior applied to observations of a GRMHD simulation with flux extending beyond the ring may be too constraining and cause over-estimation of the diameter. Reassuringly, priors that are less constraining or more accurate dependably recover the diameter, orientation, and asymmetry. On the other hand, features like the ring width and fractional central brightness can be adjusted by imposing different priors.

6.2. Ring features of M87* reconstructions

Fig. 12 and Tab. 4 show the results of feature extraction for the M87* image reconstructions. Tab. 4 includes the results of using the eht-imaging algorithm with fiducial parameters (Collaboration et al. 2019b) for reference, although eht-imaging is not directly comparable to our score-based priors since it utilizes hand-crafted regularizers as a proxy

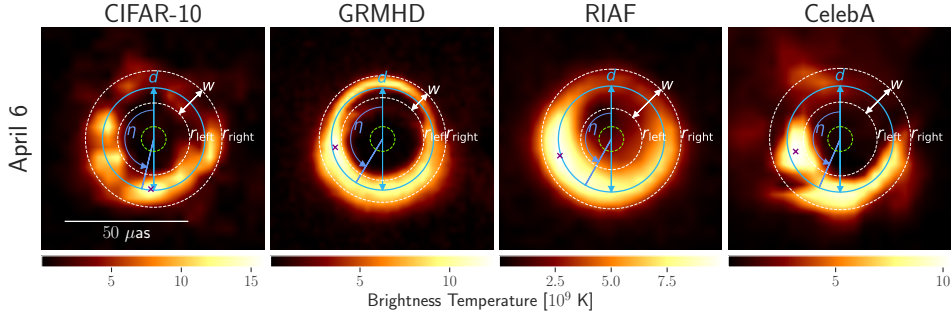


Figure 11. Visualization of extracted ring features of M87* images. Shown is a random sample (centered by REx) from each posterior for April 6. d is the ring diameter; w is the ring width. r_{left} and r_{right} delimit the radial FWHM used to estimate the orientation angle and asymmetry. η is the orientation angle measured east of north. The purple “x” marks the location of peak brightness. Asymmetry A and fractional central brightness f_C are not visualized. The green dashed circle demarcates the inner disk of radius $5 \mu\text{as}$ used to define f_C .

for a prior and visibility amplitudes instead of closure amplitudes. Fig. 11 visualizes the ring features on April 6 reconstructions. We assumed ring structure in all the posterior samples under the different score-based priors. As shown in Figs. 3 and 5, the CelebA images have the weakest ring structure, which may have caused higher variance in the extracted features.

The CIFAR-10 prior recovers a mean diameter of 41.2 to $42.5 \mu\text{as}$ across the four observations days. Accounting for error bars, all score-based priors agree on a range of possible diameters, roughly between 35 and $48 \mu\text{as}$. The diameters recovered by our score-based priors are consistent with the diameter recovered by eht-imaging, although with slightly higher means and larger error bars. Like with the simulated data, the RIAF prior leads to the highest diameters. Combined with the fact that the RIAF prior has the highest χ^2 values in Tab. 1, this suggests that the RIAF model is likely too constraining for M87*.

The ring width depends on the prior, with the GRMHD prior resulting in the lowest width (about $9 \mu\text{as}$). The RIAF prior causes the largest width (about $17 \mu\text{as}$), which is only slightly larger than the width recovered by eht-imaging (about $16 \mu\text{as}$, as listed in Tab. 4).

The orientation angle is consistent across the priors, roughly ranging from 150° on April 5 to 170° on April 11. Like previous work, we find that both the diameter and orientation angle have an upward trend over the observation days as brightness shifts to the southwest (Collaboration et al. 2019b,c).

The amount of asymmetry is also roughly consistent across the priors. Interestingly, there is most discrepancy between the priors in the April 10 reconstructions. April 10 is the day with fewest observations, which may cause the brightness asymmetry to be more flexible under the data.

As expected, the fractional central brightness varies significantly with the prior. As with the simulated data, the GRMHD prior achieves the greatest brightness contrast.

Overall, the conclusions regarding the effects of priors on the M87* reconstructions are consistent with the conclusions of previous analyses (Collaboration et al. 2019b,c) and our simulated-data analysis. The diameter, orientation, and asymmetry are robust to the prior, although some priors result in greater variability than others. There is a slight upward bias in diameter from the RIAF prior due to wider rings that account for all the flux in one RIAF model. The most prior-dependent features are the width and fractional central brightness.

7. DISCUSSION

We have presented a strategy for probing the influence of different priors on imaging from EHT VLBI data. Our imaging approach allows one to infer a diverse collection of image posteriors, each incorporating different assumptions. From these results, one can analyze the effect of the prior on the visual quality and uncertainty of reconstructed images, as well as on the recovered ring features. We applied this strategy to EHT observations of M87* and found that a GRMHD prior is most effective at recovering a visually-detailed image with a thin ring and sharp contrast. However, it exhibits less posterior uncertainty than some other priors do, meaning that one should only trust the GRMHD reconstructions if one believes in the existence of an underlying compact ring structure. On the other hand,

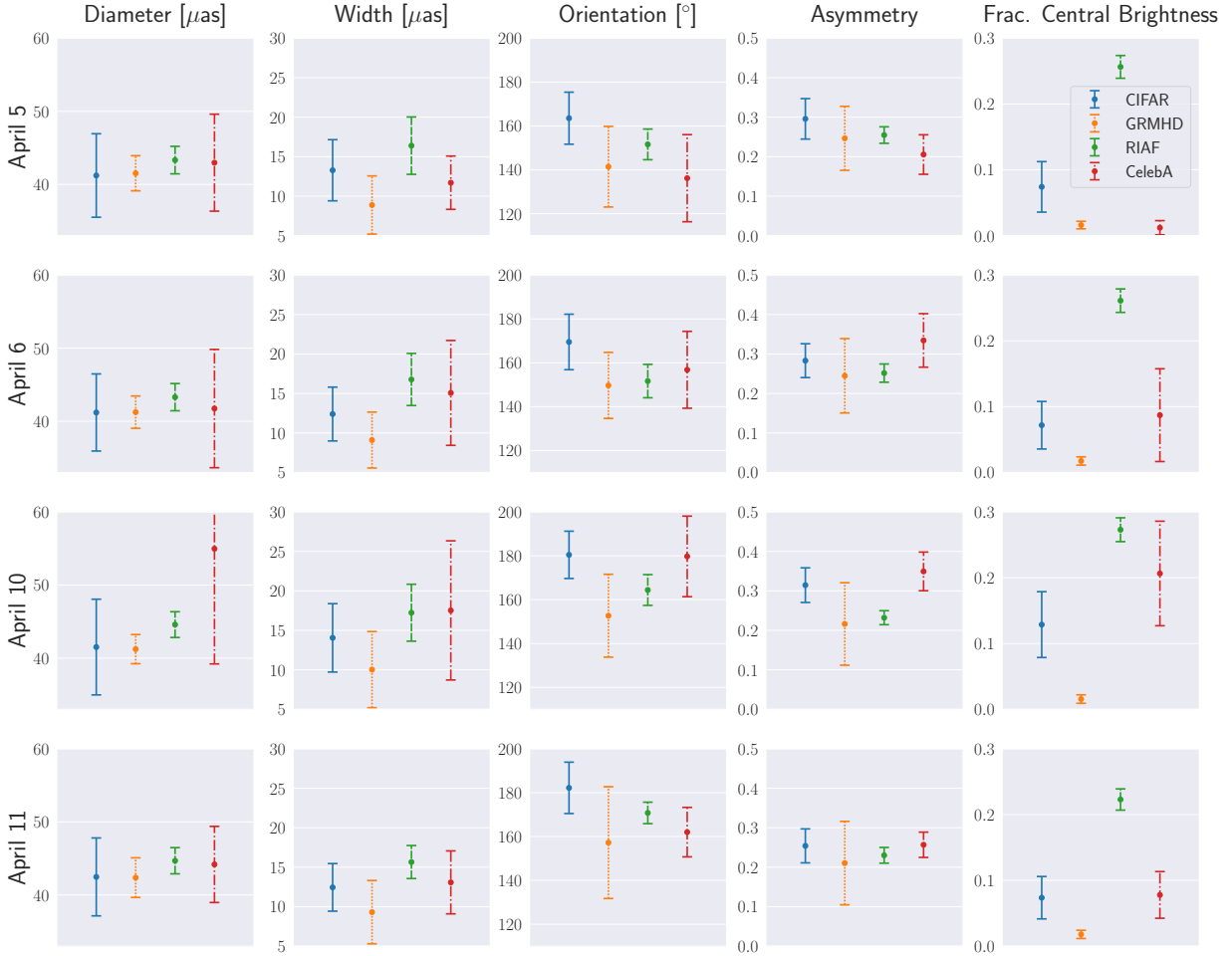


Figure 12. Extracted ring features of M87* images. The means and error bars were computed the same way as for Fig. 10. The different priors (CIFAR, GRMHD, RIAF, CelebA) all agree on the diameter, orientation, and asymmetry up to error bars. There is some disagreement in asymmetry for April 10, which is the day with fewest observations. We note a slight upward trend in diameter and orientation angle over the observation days. The width and fractional central brightness change with the prior, with the GRMHD prior providing the thinnest rings and most brightness contrast. Please see Fig. 3 for image samples.

it is possible to allow for more flexibility in the posterior with a weaker prior. For example, a CIFAR-10 prior still recovers a ring with similar diameter, orientation, and brightness asymmetry, albeit with blurrier quality. Our proposed strategy allows scientists to reliably interpret reconstructed images and account for the role of prior assumptions in their analysis.

- 1 This work was funded by NSF 2048237, 2034306, and 1935980 and the Amazon AI4Science Partnership Discovery
- 2 Grant. BTF is supported by the NSF GRFP. The authors thank Charles Gammie, Ben Prather, Abhishek Joshi, Vedant
- 3 Dhruv, and CK Chan for sharing their GRMHD simulations, as well as Aviad Levis for many helpful discussions.

APPENDIX

A. FLUX CONSTRAINT AND DATA ANNEALING

As mentioned in Sec. 3, we make two additions to a vanilla VI approach: a flux-constraint objective and a data-weight annealing schedule. Fig. 13 demonstrates the effect of each addition through an ablation study. A flux constraint imposes the assumption that all posterior images have the same total flux, which reduces the complexity of the posterior

	eht-imaging*	CIFAR-10	GRMHD	RIAF	CelebA
Diameter [μs]					
April 5	39.3 ± 1.6	41.2 ± 5.7	41.5 ± 2.4	43.3 ± 1.9	43.0 ± 6.6
April 6	39.5 ± 1.5	41.2 ± 5.3	41.2 ± 2.2	43.3 ± 1.9	41.7 ± 8.1
April 10	40.5 ± 1.3	41.5 ± 6.5	41.2 ± 2.0	44.6 ± 1.8	55.0 ± 15.8
April 11	41.1 ± 1.2	42.5 ± 5.3	42.4 ± 2.7	44.7 ± 1.8	44.2 ± 5.2
Width [μs]					
April 5	16.3 ± 1.5	13.3 ± 3.9	8.9 ± 3.7	16.4 ± 3.6	11.7 ± 3.4
April 6	16.2 ± 1.0	12.4 ± 3.4	9.1 ± 3.5	16.8 ± 3.3	15.1 ± 6.6
April 10	15.7 ± 1.3	14.1 ± 4.3	10.0 ± 4.8	17.2 ± 3.6	17.5 ± 8.8
April 11	15.6 ± 0.9	12.4 ± 3.0	9.3 ± 4.0	15.7 ± 2.1	13.1 ± 4.0
Orientation [$^\circ$]					
April 5	149.0 ± 4.0	163.5 ± 11.9	141.4 ± 18.4	151.6 ± 7.0	136.2 ± 19.9
April 6	151.2 ± 3.2	169.5 ± 12.6	149.7 ± 15.1	151.7 ± 7.6	156.8 ± 17.5
April 10	171.1 ± 3.4	180.4 ± 10.8	152.7 ± 18.9	164.4 ± 7.0	179.7 ± 18.4
April 11	167.5 ± 3.1	182.2 ± 11.7	157.2 ± 25.5	170.8 ± 4.9	162.0 ± 11.3
Asymmetry					
April 5	0.25 ± 0.01	0.30 ± 0.05	0.25 ± 0.08	0.25 ± 0.02	0.21 ± 0.05
April 6	0.24 ± 0.02	0.28 ± 0.04	0.24 ± 0.09	0.25 ± 0.02	0.33 ± 0.07
April 10	0.23 ± 0.00	0.31 ± 0.04	0.22 ± 0.10	0.23 ± 0.02	0.35 ± 0.05
April 11	0.20 ± 0.01	0.25 ± 0.04	0.21 ± 0.11	0.23 ± 0.02	0.26 ± 0.03
Frac. Central Brightness					
April 5	0.07	0.07 ± 0.04	0.02 ± 0.01	0.26 ± 0.02	0.01 ± 0.01
April 6	0.07	0.07 ± 0.04	0.02 ± 0.01	0.26 ± 0.02	0.09 ± 0.07
April 10	0.04	0.13 ± 0.05	0.02 ± 0.01	0.27 ± 0.02	0.21 ± 0.08
April 11	0.04	0.07 ± 0.03	0.02 ± 0.01	0.22 ± 0.02	0.08 ± 0.04

Table 4. Extracted ring features of M87* images. This table reports the means and std. devs. that are visualized in Fig. 12. *eht-imaging is not exactly comparable to the score-based priors because it is a different imaging algorithm that uses hand-crafted regularizers instead of a data-driven prior. There are small differences from the values for eht-imaging reported in Table 7 of Collaboration et al. (2019b). This may be due to differences in implementation/hardware and in the exact definitions of the features (see Appendix D for details).

distribution. Data annealing helps prevent falling into bad local minima when optimizing the variational distribution (Eq. 7), since the magnitude of the data loss is much higher than the magnitude of the prior loss at the beginning of optimization. As Fig. 13 shows, both additions help make optimization more stable.

A.1. Flux constraint

Recall that a flux constraint is imposed through the following objective term in Eq. 7:

$$\mathcal{L}_{\text{flux}}(\mathbf{x}) = (V(\mathbf{x}) - \bar{V})^2, \quad (\text{A1})$$

where $V(\mathbf{x})$ is the total flux of the image \mathbf{x} , and \bar{V} is the target total flux.

The flux constraint should be considered an additional prior on top of the score-based prior. It imposes the assumption of a constant total flux across the posterior (since closure quantities in the log-likelihood do not constrain total flux). The value of \bar{V} also influences the posterior: a lower \bar{V} encourages sparser, more-compact images than a higher \bar{V} . Fig. 14 demonstrates this when using the CelebA prior on simulated data of the Crescent image.

Our approach is to set \bar{V} according to the preferred total flux of the score-based prior. That is, we set it as the median total flux of 512 samples from the prior. This results in $\bar{V} = 38, 173, 90$, and 112 for the CIFAR-10, GRMHD,

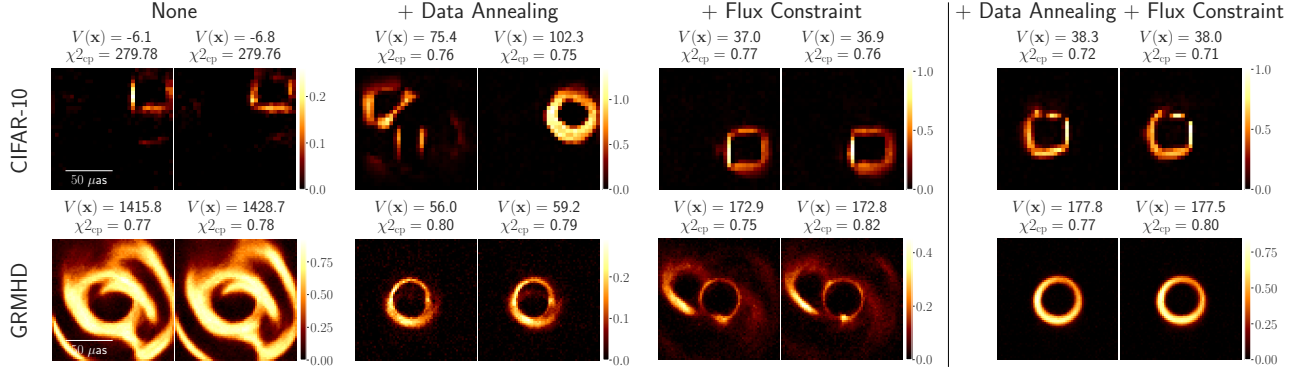


Figure 13. Ablation of data annealing and flux constraint. The simulated measurements are of the Crescent image in Fig. 6. The posterior samples are shown with their original number of pixels (i.e., 32×32 or 64×64) and with their original pixel values (which should be between 0 and 1). “None” is vanilla optimization without data-weight annealing or a flux-constraint objective. Without a flux constraint, the total flux $V(\mathbf{x})$ of samples varies widely; furthermore, a posterior that is unconstrained in the total flux may be too complicated to model with VI. Without data annealing, optimization may become unstable, as is the case for the GRMHD prior here. Optimization is generally more stable when both data annealing and a flux constraint are used.

RIAF, and CelebA priors, respectively. Images can be scaled to the actual target flux \bar{V}_{orig} measured by the zero-baseline (e.g., $\bar{V}_{\text{orig}} = 0.6$ Jy) by a factor of $\bar{V}_{\text{orig}}/\bar{V}$. By setting \bar{V} based on the score-based prior, we attempt to make most of the image-reconstruction bias come from the score-based prior rather than from the target flux.

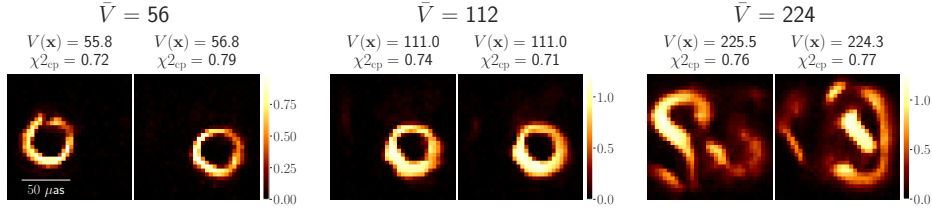


Figure 14. Effect of target flux \bar{V} . The simulated measurements are of the Crescent image in Fig. 6, and the prior is the CelebA score-based prior. $\bar{V} = 112$ is the default target total flux chosen based on samples from the prior. When \bar{V} is halved to 56, the estimated posterior images are sparser. When \bar{V} is doubled to 224, the estimated posterior images have less compactness. $\bar{V} = 112$ is essentially the preferred total flux under the score-based prior.

A.2. Data annealing

The variational distribution is randomly initialized to solve the VI optimization problem (Eq. 7), which means the data loss, or negative log-likelihood, is quite high at the beginning of optimization. This can cause convergence to posterior samples that are not preferred by the score-based prior (see the GRMHD example in Fig. 13 when only a flux constraint is used). To avoid poor local minima, we initialize the weight of the data loss at 0 and then gradually anneal it to 1 with the following annealing schedule:

$$\lambda_{\text{data}}(i) = \frac{1}{1 + \exp(-r(i - s))}, \quad (\text{A2})$$

where $i \in \mathbb{Z}^+$ is the optimization step, $r \in [0, 1]$ is the annealing rate, and $s \in \mathbb{Z}^+$ is the pivot step at which $\lambda_{\text{data}}(i) = 0.5$. We use $r = 0.002$ and $s = 12000$. Therefore, strictly speaking, our optimization approach is to iteratively apply the gradient of the following loss function with respect to the RealNVP parameters ϕ at each step i :

$$\mathcal{L}(\phi, i) := \mathbb{E}_{\mathbf{x} \sim q_\phi} \left[\lambda_{\text{data}}(i) (-\log p(\mathbf{y}_{\text{cp}} | \mathbf{x}) - \log p(\mathbf{y}_{\text{logca}} | \mathbf{x})) - b_\theta(\mathbf{x}) + (V(\mathbf{x}) - \bar{V})^2 + \log q_\phi(\mathbf{x}) \right]. \quad (\text{A3})$$

Since we run optimization for 100k steps, $\lambda_{\text{data}}(i)$ is mostly equal to 1 except at the very beginning of optimization.

B. SCORE-BASED DIFFUSION MODELS

To obtain a score-based prior, we train a score-based diffusion model with parameters θ on samples from the target prior p_{data} . Once trained, the diffusion model can sample from a learned distribution $p_\theta \approx p_{\text{data}}$. In this appendix, we provide technical background on score-based diffusion models and how to evaluate p_θ .

B.1. Score-based diffusion models

A score-based diffusion model learns to gradually denoise samples from the tractable distribution $\pi = \mathcal{N}(\mathbf{0}, \mathbf{I})$ into samples from a clean image distribution p_{data} . Denoising is treated as a continuous-time process such that an image is a time-dependent variable $\mathbf{x}(t)$ for $t \in [0, T]$. A higher t corresponds to higher independent Gaussian noise in $\mathbf{x}(t)$. The following stochastic differential equation (SDE) dictates how $\mathbf{x}(t)$ is “diffused” as t goes from 0 to T :

$$d\mathbf{x} = \mathbf{f}(\mathbf{x}, t) + g(t)d\mathbf{w}, \quad t \in [0, T]. \quad (\text{B4})$$

Here $\mathbf{w} \in \mathbb{R}^D$ is a standard Brownian motion, $\mathbf{f}(\cdot, t) : \mathbb{R}^D \rightarrow \mathbb{R}^D$ is the drift coefficient that controls the deterministic evolution of $\mathbf{x}(t)$, and $g(t) \in \mathbb{R}$ is the diffusion coefficient that controls the rate of noise increase in $\mathbf{x}(t)$. (Note that $\mathbf{f}(\cdot, t)$ here is distinct from the forward model $\mathbf{f}(\cdot)$ in Sec. 2.1.) The stochastic trajectory $\{\mathbf{x}(t)\}_{t=0}^T$ gives rise to a time-dependent marginal probability distribution p_t . $\mathbf{f}(\cdot, t)$ and $g(t)$ are constructed such that if $p_0 = p_{\text{data}}$, then $p_T \approx \pi$.

A diffusion model learns to *reverse* the diffusion process. One can sample from the complicated distribution p_{data} by first sampling from the tractable π distribution and then using the diffusion model to transform those samples into clean images from p_{data} . The reverse of the diffusion process is given by the following reverse-time SDE:

$$d\mathbf{x} = [\mathbf{f}(\mathbf{x}, t) - g(t)^2 \nabla_{\mathbf{x}} \log p_t(\mathbf{x})] dt + g(t)d\bar{\mathbf{w}}, \quad t \in [0, T]. \quad (\text{B5})$$

The gradient $\nabla_{\mathbf{x}} \log p_t(\mathbf{x})$ is known as the *Stein score* (Stein 1972) of \mathbf{x} under p_t , and it helps bring noisy images closer to the clean image distribution. It is also the component in Eq. B5 that is learned by the diffusion model. A convolutional neural network with parameters θ , known as the *score model* \mathbf{s}_θ , is trained to approximate the true score such that $\mathbf{s}_\theta(\mathbf{x}, t) \approx \nabla_{\mathbf{x}} \log p_t(\mathbf{x})$. The score model appears in the following learned approximation of Eq. B5, which is used to sample from an approximation of p_{data} :

$$d\mathbf{x} = [\mathbf{f}(\mathbf{x}, t) - g(t)^2 \mathbf{s}_\theta(\mathbf{x}, t)] dt + g(t)d\bar{\mathbf{w}}, \quad t \in [0, T]. \quad (\text{B6})$$

For $\mathbf{x}(T) \sim \pi$, we denote the time-dependent marginal distribution of $\mathbf{x}(t)$ according to Eq. B6 as \hat{p}_t . We denote the diffusion-model prior as $p_\theta := \hat{p}_0$. For a well-trained score model, we have that $p_\theta \approx p_{\text{data}}$.

B.2. Image probabilities under a score-based diffusion model

To use p_θ as a prior in an inference algorithm that optimizes the posterior log-density, we need access to the function $\log p_\theta(\cdot)$. Computing the probability of an image \mathbf{x} under p_θ requires inverting $\mathbf{x}(0) = \mathbf{x}$ to $\mathbf{x}(T)$ (i.e., we need to find the $\mathbf{x}(T)$ that would result in $\mathbf{x}(0)$ through the reverse diffusion defined by Eq. B6). However, although we can use Eq. B6 to sample from p_θ , the presence of Brownian motion makes the sampling function not invertible. As a result, there is no tractable way to compute $\log p_\theta(\mathbf{x})$. Instead, we can appeal to an ordinary differential equation (ODE) for tractable log-probabilities or to the evidence lower bound (ELBO) as an efficient proxy.

B.2.1. Computing probabilities with an ODE

The following *probability flow ODE* defines a generative image distribution p_θ^{ODE} theoretically equal to p_θ :

$$\frac{d\mathbf{x}}{dt} = \mathbf{f}(\mathbf{x}, t) - \frac{1}{2}g(t)^2 \mathbf{s}_\theta(\mathbf{x}, t) := \tilde{\mathbf{f}}_\theta(\mathbf{x}, t). \quad (\text{B7})$$

Like the reverse-time SDE, this ODE can be used to sample $\mathbf{x}(0) \sim p_\theta^{\text{ODE}}$ by starting with $\mathbf{x}(T) \sim \pi$. Furthermore, an ODE can be solved in both directions of time, making the sampling function invertible. To compute $\log p_\theta^{\text{ODE}}(\mathbf{x})$ for an image \mathbf{x} , we map $\mathbf{x}(0) = \mathbf{x}$ to $\mathbf{x}(T)$ by solving the ODE in the forward time direction. The log-probability is given by the log-probability of $\mathbf{x}(T)$ under π (which is tractable to evaluate) plus a normalization factor accounting for the change in log-density throughout the ODE:

$$\log p_\theta^{\text{ODE}}(\mathbf{x}(0)) = \log \pi(\mathbf{x}(T)) + \int_0^T \nabla \cdot \tilde{\mathbf{f}}_\theta(\mathbf{x}(t), t) dt, \quad \mathbf{x}(0) = \mathbf{x}. \quad (\text{B8})$$

Eq. B8 is tractable to evaluate with an ODE solver, but it is computationally expensive. It can be prohibitively expensive when the image is large or when used in an iterative optimization algorithm.

B.2.2. Surrogate probabilities with an evidence lower bound

Song et al. (Song et al. 2021a) derived the evidence lower bound b_θ of a score-based diffusion model such that $b_\theta(\mathbf{x}) \leq \log p_\theta(\mathbf{x})$ for any \mathbf{x} . The lower-bound, which is similar to the denoising-based training objective of diffusion models, is given by

$$b_\theta(\mathbf{x}) := \mathbb{E}_{p_{0T}(\mathbf{x}'|\mathbf{x})} [\log \pi(\mathbf{x}')] - \frac{1}{2} \int_0^T g(t)^2 h(\mathbf{x}, t) dt, \quad (\text{B9})$$

where

$$h(\mathbf{x}, t) := \mathbb{E}_{p_{0t}(\mathbf{x}'|\mathbf{x})} \left[\|\mathbf{s}_\theta(\mathbf{x}', t) - \nabla_{\mathbf{x}'} \log p_{0t}(\mathbf{x}' | \mathbf{x})\|_2^2 - \|\nabla_{\mathbf{x}'} \log p_{0t}(\mathbf{x}' | \mathbf{x})\|_2^2 - \frac{2}{g(t)^2} \nabla_{\mathbf{x}'} \cdot \mathbf{f}(\mathbf{x}', t) \right]. \quad (\text{B10})$$

$p_{0t}(\mathbf{x}' | \mathbf{x})$ denotes the transition distribution of $\mathbf{x}(t) = \mathbf{x}'$ given $\mathbf{x}(0) = \mathbf{x}$ under the diffusion SDE (Eq. B4). In denoising diffusion models, which use a linear drift coefficient $\mathbf{f}(\cdot, t)$, this transition distribution is Gaussian: $p_{0t}(\mathbf{x}' | \mathbf{x}) = \mathcal{N}(\mathbf{x}'; \alpha(t)\mathbf{x}, \beta(t)^2\mathbf{I})$. This in turn makes $\int_0^T g(t)^2 h(\mathbf{x}, t) dt$ similar to a denoising score-matching objective. In fact, Eq. B9 is known as the ‘‘denoising score-matching loss’’ in the original theoretical work (Song et al. 2021a).

To see the correspondence to denoising, note that for $p_{0t}(\mathbf{x}' | \mathbf{x}) = \mathcal{N}(\mathbf{x}'; \alpha(t)\mathbf{x}, \beta(t)^2\mathbf{I})$, we can sample \mathbf{x}' as $\alpha_t\mathbf{x} + \beta_t\mathbf{z}$ for $\mathbf{z} \sim \mathcal{N}(\mathbf{0}, \mathbf{I})$. Then the gradient $\nabla_{\mathbf{x}'} \log p_{0t}(\mathbf{x}' | \mathbf{x})$ in Eq. B10 is given by

$$\nabla_{\mathbf{x}'} \log p_{0t}(\mathbf{x}' | \mathbf{x}) = -\frac{1}{\beta_t^2}(\mathbf{x}' - \alpha_t\mathbf{x}) = -\frac{\mathbf{z}}{\beta_t}. \quad (\text{B11})$$

The first term in Eq. B10, $\|\mathbf{s}_\theta(\mathbf{x}', t) - \nabla_{\mathbf{x}'} \log p_{0t}(\mathbf{x}' | \mathbf{x})\|_2^2$, thus can be thought-of as the denoising error of the score model. A lower error corresponds to a higher ELBO according to Eq. B9. The remaining two terms in Eq. B10 are normalizing factors independent of θ . Loosely speaking, the ELBO indicates how well the diffusion model can denoise the given image: an image with high probability under the diffusion model is easy to denoise, whereas a low-probability image is difficult to denoise.

$b_\theta(\mathbf{x})$ is efficient to compute by adding Gaussian noise to \mathbf{x} and seeing how well the score model estimates the noise. We Monte-Carlo approximate the expectation over $p_{0T}(\mathbf{x}' | \mathbf{x})$ with $N_{\mathbf{z}}$ noise samples, and we Monte-Carlo approximate the time integral in Eq. B9 with importance sampling of N_t time samples. In practice, $N_{\mathbf{z}} = N_t = 1$ is sufficient for our imaging algorithm.

C. INTERFEROMETRIC DATA PRODUCTS

In this appendix, we provide background on the data products obtained with VLBI. In VLBI, a network of radio telescopes collects spatial-frequency measurements of the sky’s image. We denote the source image as $I(x, y)$, where (x, y) are 2D spatial coordinates. Each pair of telescopes is called a *baseline* and provides a Fourier measurement called a *visibility*. The *van Cittert-Zernike Theorem* (van Cittert 1934; Zernike 1938) states that the ideal visibility v_{ij}^* measured by the baseline \mathbf{b}_{ij} between telescopes i and j is a single (u, v) measurement on the complex 2D Fourier plane (Thompson et al. 2017):

$$v_{ij}^* := \tilde{I}(u, v) = \int \int I(x, y) e^{-2\pi i(xu + yv)} dx dy. \quad (\text{C12})$$

(Here i is used to denote the imaginary unit to avoid confusion with the telescope index i .) The coordinates (u, v) (measured in wavelengths) are the projected baseline orthogonal to the line of sight. An array of N_s telescopes, or stations, has $\binom{N_s}{2}$ independent baselines, each providing a visibility at each point in time.

In practice, ideal visibilities are corrupted due to multiple factors: (1) baseline-dependent thermal noise, (2) station-dependent gain errors, and (3) station-dependent phase errors. Baseline-dependent **thermal noise** is modeled as a Gaussian random variable $\varepsilon_{ij} \sim \mathcal{N}(0, \sigma_{ij}^2)$, where σ_{ij} is based on the system equivalent flux density (SEFD) of each telescope: $\sigma_{ij} \propto \sqrt{\text{SEFD}_i + \text{SEFD}_j}$. The **station-dependent gain error** g_i arises from each telescope i using its own time-dependent 2×2 Jones matrix (Hamaker et al. 1996). The **station-dependent phase error** ϕ_i

arises from atmospheric turbulence that causes light to travel at different velocities toward each telescope (Hinder 1970; Kolmogorov 1991; Taylor 1938). Other sources of corruption, including polarization leakage and bandpass errors, may introduce baseline-dependent errors, but they are slow-varying and assumed to be removable with *a priori* calibration (Chael et al. 2018). The measured visibility of baseline \mathbf{b}_{ij} can be written as

$$v_{ij} = g_i g_j e^{i(\phi_i - \phi_j)} v_{ij}^* + \varepsilon_{ij}, \quad (\text{C13})$$

where all systematic errors (i.e., those besides thermal noise) are wrapped into station-dependent gain/phase errors.

C.1. Closure quantities

Station-dependent errors are difficult to remove due to the absence of corroborating information from other stations. Calibrating the measured visibilities calls for an iterative self-calibration process that introduces many *a priori* assumptions and becomes infeasible at high telescope frequencies (Chael et al. 2018). An alternative avenue is to use closure quantities that are unchanged by station-dependent errors.

Closure phases (Jennison 1958) are robust to station-dependent phase errors. They arise from a data product known as the complex *bispectrum*, which is formed by multiplying the three baselines within a triangle of telescopes i, j, k :

$$v_{ij} v_{jk} v_{ki} = \left(g_i g_j e^{i(\phi_i - \phi_j)} v_{ij}^* + \varepsilon_{ij} \right) \left(g_j g_k e^{i(\phi_j - \phi_k)} v_{jk}^* + \varepsilon_{jk} \right) \left(g_k g_i e^{i(\phi_k - \phi_i)} v_{ki}^* + \varepsilon_{ki} \right) \quad (\text{C14})$$

$$= g_{ijk}^2 e^{i(\phi_i - \phi_j)} e^{i(\phi_j - \phi_k)} e^{i(\phi_k - \phi_i)} v_{ij}^* v_{jk}^* v_{ki}^* + \varepsilon_{ijk} \quad (\text{C15})$$

$$= g_{ijk}^2 v_{ij}^* v_{jk}^* v_{ki}^* + \varepsilon_{ijk}, \quad (\text{C16})$$

where ε_{ijk} is the thermal noise in the measured bispectrum. Importantly, Eq. C16 does not include any phase errors. Thus the closure phase is given by the phase of the bispectrum and is robust to phase corruption. While the total number of triplets in the telescope array is $\binom{N_s}{3}$, the total number of linearly independent closure phases is $N_{\text{cp}} = \binom{N_s - 1}{2}$. To understand this number, see that the set of independent closure phases can be formed by selecting one station as a reference and then creating the set of all triangles that contain that station. The resulting closure phases are independent in that no one closure phase can be formed as a linear combination of other closure phases.

Closure amplitudes (Twiss et al. 1960) address the issue of station-dependent gain errors. A closure amplitude arises from a combination of four telescopes i, j, k, ℓ :

$$\frac{v_{ij} v_{kl}}{v_{ik} v_{jl}} = \frac{\left(g_i g_j e^{i(\phi_i - \phi_j)} v_{ij}^* + \varepsilon_{ij} \right) \left(g_k g_\ell e^{i(\phi_k - \phi_\ell)} v_{kl}^* + \varepsilon_{kl} \right)}{\left(g_i g_k e^{i(\phi_i - \phi_k)} v_{ik}^* + \varepsilon_{ik} \right) \left(g_j g_\ell e^{i(\phi_j - \phi_\ell)} v_{j\ell}^* + \varepsilon_{j\ell} \right)} \quad (\text{C17})$$

$$= \frac{g_i g_j g_k g_\ell e^{i(\phi_i - \phi_j)} e^{i(\phi_k - \phi_\ell)} v_{ij}^* v_{kl}^*}{g_i g_j g_k g_\ell e^{i(\phi_i - \phi_k)} e^{i(\phi_j - \phi_\ell)} v_{ik}^* v_{j\ell}^*} + \varepsilon_{ijk\ell} \quad (\text{C18})$$

$$= e^{2i(\phi_k - \phi_j)} \frac{v_{ij}^* v_{kl}^*}{v_{ik}^* v_{j\ell}^*} + \varepsilon_{ijk\ell}, \quad (\text{C19})$$

where $\varepsilon_{ijk\ell}$ is the thermal noise in the closure amplitude. Eq. C19 does not depend on station-dependent gain errors, so the amplitude $\left| \frac{v_{ij} v_{kl}}{v_{ik} v_{jl}} \right|$ is taken as the closure amplitude. In this work, we use the log of the closure amplitude. The number of linearly independent log closure amplitudes is $N_{\text{logca}} = \binom{N_s(N_s - 3)}{2}$.

D. RING FEATURE EXTRACTION

We used the REx feature extraction algorithm (Chael 2019) to compute the characteristic features in Sec. 6. The diameter and fractional central brightness follow the same formulae as in Collaboration et al. (2019b). Except for the fractional central brightness, which is not included in REx, all features were computed exactly according to the latest implementation of REx³ (as of October 2023). The REx implementation corresponds to slightly different equations for computing features than those given in Collaboration et al. (2019b). In this appendix, we will note any differences from the equations used in Collaboration et al. (2019b).

³ <https://github.com/achael/eht-imaging/blob/main/ehtim/features/rex.py>

REx first pre-processes the image by blurring it with a $2 \mu\text{as}$ FWHM Gaussian and re-gridding it to 160×160 pixels. It identifies the ring center based on the image thresholded to 5% of the peak brightness, and then it computes characteristic features. The characteristic features, which we define in the following paragraphs, are all computed based on radial-angular profiles $I(r, \theta)$ of the centered image, where $I(r, \theta)$ is the brightness at radius r and azimuthal angle θ from the measured center. The profiles are interpolated over the domains $r \in [0, 50] \mu\text{as}$ and $\theta \in [0, 2\pi]$ radians.

The diameter d is measured as twice the mean radial distance of the peak brightness:

$$d = 2 \langle r_{\text{pk}}(\theta) \rangle_{\theta \in [0, 2\pi]} := 2 \left\langle \arg \max_r I(r, \theta) \right\rangle_{\theta \in [0, 2\pi]}, \quad (\text{D20})$$

where $\langle \cdot \rangle_{\theta \in [0, 2\pi]}$ denotes the mean over the domain $\theta \in [0, 2\pi]$. The uncertainty of the diameter is given as the corresponding standard deviation. This equation for d exactly agrees with Eq. 18 in Collaboration et al. (2019b).

The width w is measured as the mean FWHM of radial slices:

$$w = \langle \text{FWHM}(I(r, \theta)) \rangle_{\theta \in [0, 2\pi]}, \quad (\text{D21})$$

where $\text{FWHM}(\cdot)$ evaluates the FWHM of a 1D radial profile. The uncertainty is computed as the corresponding standard deviation. Note that this is slightly different from the expression for w given in Eq. 20 in Collaboration et al. (2019b), which first subtracts the mean flux outside the ring before estimating the width.

To measure the orientation angle, REx first estimates the FWHM of the mean radial profile with zero-mean outside flux, defined as

$$\text{FWHM}(\bar{I}(r) - I_{\text{floor}}),$$

where $\bar{I}(r) := \langle I(r, \theta) \rangle_{\theta \in [0, 2\pi]}$, and $I_{\text{floor}} := \langle I(r = 50, \theta) \rangle_{\theta \in [0, 2\pi]}$. Let r_{left} and r_{right} denote the minimum and maximum radii, respectively, of this FWHM. The orientation angle is computed by finding the phase of the first angular mode of each normalized angular profile $I(r, \theta)$ at fixed r throughout the FWHM and then taking the circular mean:

$$\eta = \left\langle \angle \left[\frac{\int_0^{2\pi} I(r, \theta) e^{i\theta} d\theta}{\int_0^{2\pi} I(r, \theta) d\theta} \right] \right\rangle_{r \in [r_{\text{left}}, r_{\text{right}}]}. \quad (\text{D22})$$

The uncertainty of η is the corresponding circular standard deviation. The only difference between this equation and Eq. 21 in Collaboration et al. (2019b) comes from r_{left} and r_{right} . In Collaboration et al. (2019b), $r_{\text{in}} = (d - w)/2$ and $r_{\text{out}} = (d + w)/2$ are used instead.

The azimuthal asymmetry A is measured as the mean normalized amplitude of the same first angular modes:

$$A = \left\langle \left| \frac{\int_0^{2\pi} I(r, \theta) e^{i\theta} d\theta}{\int_0^{2\pi} I(r, \theta) d\theta} \right| \right\rangle_{r \in [r_{\text{left}}, r_{\text{right}}]}, \quad (\text{D23})$$

and the uncertainty of A is the corresponding standard deviation. Once again, the only difference from Eq. 22 in Collaboration et al. (2019b) is that r_{left} and r_{right} are used instead of r_{in} and r_{out} .

We define the fractional central brightness f_{C} (which is not included in REx) as the ratio of an ‘‘interior’’ mean flux to the mean flux along the ring:

$$f_{\text{C}} = \frac{\langle I(r, \theta) \rangle_{r \in [0, 5], \theta \in [0, 2\pi]}}{\langle I(d/2, \theta) \rangle_{\theta \in [0, 2\pi]}}. \quad (\text{D24})$$

Here the inside is defined as the inner disk of radius $5 \mu\text{as}$, and the outside is defined as the region with radius larger than the measured radius $d/2$. There is no uncertainty quantification for f_{C} . This definition of f_{C} exactly agrees with Eq. 23 in Collaboration et al. (2019b).

E. IMPLEMENTATION DETAILS

In this appendix, we provide implementation details about the approach used in our experiments.

E.1. Optimization of the RealNVP variational posterior

For the variational distribution, we used a RealNVP normalizing-flow network with 32 affine-coupling layers with a width of $D/8$ neurons in the first layer, where D is the number of pixels in the images (i.e., 32×32 or 64×64 in this work). Stochastic gradient-based optimization was done with batches of 64 images and the Adam optimizer with a learning rate of 10^{-5} and gradient clip of 1. For each posterior, we ran optimization for 100k iterations.

E.2. *Score-based prior*

For the score-based diffusion model, we used a score model with the NCSN++ architecture with 64 filters in the first layer, trained according to the Variance-Preserving (VP) SDE (Song et al. 2021b). The CIFAR-10, GRMHD, RIAF, and CelebA score-based priors were trained for 100k, 100k, 20k, and 100k iterations, respectively. The evidence lower bound $b_\theta(\mathbf{x})$ (Eq. B9) was Monte-Carlo-approximated with $N_t = 1$ time sample and $N_z = 1$ noise sample.

REFERENCES

- Adam, A., Coogan, A., Malkin, N., et al. 2022, arXiv preprint arXiv:2211.03812
- Akiyama, K., Tazaki, F., Moriyama, K., et al. 2019, *Astrophysics Source Code Library*, ascl
- Akiyama, K., Kuramochi, K., Ikeda, S., et al. 2017, *The Astrophysical Journal*, 838, 1
- Akiyama, K., Alberdi, A., Alef, W., et al. 2024, *Astronomy & Astrophysics*, 681, A79
- Arras, P., Frank, P., Haim, P., et al. 2022, *Nature Astronomy*, 6, 259
- Blackburn, L., Pesce, D. W., Johnson, M. D., et al. 2020, *The Astrophysical Journal*, 894, 31, doi: [10.3847/1538-4357/ab8469](https://doi.org/10.3847/1538-4357/ab8469)
- Bouman, K. L., Johnson, M. D., Zoran, D., et al. 2016, in *Proceedings of the IEEE Conference on Computer Vision and Pattern Recognition*, 913–922
- Broderick, A. E., Fish, V. L., Doleman, S. S., & Loeb, A. 2011, *The Astrophysical Journal*, 735, 110, doi: [10.1088/0004-637X/735/2/110](https://doi.org/10.1088/0004-637X/735/2/110)
- Broderick, A. E., & Pesce, D. W. 2020, *The Astrophysical Journal*, 904, 126, doi: [10.3847/1538-4357/abbd9d](https://doi.org/10.3847/1538-4357/abbd9d)
- Chael, A. A. 2019, PhD thesis, Harvard University
- Chael, A. A., Johnson, M. D., Bouman, K. L., et al. 2018, *The Astrophysical Journal*, 857, 23, doi: [10.3847/1538-4357/aab6a8](https://doi.org/10.3847/1538-4357/aab6a8)
- Chael, A. A., Johnson, M. D., Narayan, R., et al. 2016, *The Astrophysical Journal*, 829, 11
- Choi, J., Kim, S., Jeong, Y., Gwon, Y., & Yoon, S. 2021, in *ICCV*, IEEE
- Chung, H., Kim, J., McCann, M. T., Klasky, M. L., & Ye, J. C. 2023, in *The Eleventh International Conference on Learning Representations*. <https://openreview.net/forum?id=OnD9zGAGT0k>
- Chung, H., Sim, B., Ryu, D., & Ye, J. C. 2022a, arXiv preprint arXiv:2206.00941
- Chung, H., Sim, B., & Ye, J. C. 2022b, in *Proceedings of the IEEE/CVF Conference on Computer Vision and Pattern Recognition*, 12413–12422
- Chung, H., & Ye, J. C. 2022, *Medical Image Analysis*, 80, 102479
- Clark, B. 1980, *Astronomy and Astrophysics*, vol. 89, no. 3, Sept. 1980, p. 377, 378., 89, 377
- Collaboration, E. H. T., Akiyama, K., Alberdi, A., et al. 2022, *The Astrophysical Journal Letters*, 930, L14, doi: [10.3847/2041-8213/ac6429](https://doi.org/10.3847/2041-8213/ac6429)
- Collaboration, T. E. H. T., Akiyama, K., Alberdi, A., et al. 2019a, *The Astrophysical Journal Letters*, 875, L1, doi: [10.3847/2041-8213/ab0ec7](https://doi.org/10.3847/2041-8213/ab0ec7)
- . 2019b, *The Astrophysical Journal Letters*, 875, L4, doi: [10.3847/2041-8213/ab0e85](https://doi.org/10.3847/2041-8213/ab0e85)
- . 2019c, *The Astrophysical Journal Letters*, 875, L6, doi: [10.3847/2041-8213/ab1141](https://doi.org/10.3847/2041-8213/ab1141)
- . 2019d, *The Astrophysical Journal Letters*, 875, L2, doi: [10.3847/2041-8213/ab0c96](https://doi.org/10.3847/2041-8213/ab0c96)
- . 2019e, *The Astrophysical Journal Letters*, 875, L3, doi: [10.3847/2041-8213/ab0c57](https://doi.org/10.3847/2041-8213/ab0c57)
- . 2019f, *The Astrophysical Journal Letters*, 875, L5, doi: [10.3847/2041-8213/ab0f43](https://doi.org/10.3847/2041-8213/ab0f43)
- Cornwell, T., Braun, R., & Briggs, D. S. 1999, in *Synthesis Imaging in Radio Astronomy II*, Vol. 180, 151
- Dhariwal, P., & Nichol, A. 2021, *Advances in neural information processing systems*, 34, 8780
- Dia, N., Yantovski-Barth, M., Adam, A., et al. 2023, arXiv preprint arXiv:2311.18012
- Dinh, L., Sohl-Dickstein, J., & Bengio, S. 2016, arXiv preprint arXiv:1605.08803
- Falcke, H., Melia, F., & Agol, E. 1999, *The Astrophysical Journal*, 528, L13, doi: [10.1086/312423](https://doi.org/10.1086/312423)
- Feng, B. T., & Bouman, K. L. 2023, arXiv preprint arXiv:2309.01949
- Feng, B. T., Smith, J., Rubinstein, M., et al. 2023, in *International Conference on Computer Vision (ICCV)*, IEEE
- Gebhardt, K., Adams, J., Richstone, D., et al. 2011, *The Astrophysical Journal*, 729, 119
- Graikos, A., Malkin, N., Jojic, N., & Samaras, D. 2022, in *Thirty-Sixth Conference on Neural Information Processing Systems*. <https://arxiv.org/pdf/2206.09012.pdf>
- Hamaker, J., Bregman, J., & Sault, R. 1996, *Astronomy and Astrophysics Supplement Series*, 117, 137
- Hinder, R. 1970, *Nature*, 225, 614
- Ho, J., Jain, A., & Abbeel, P. 2020, *Advances in neural information processing systems*, 33, 6840

- Högbom, J. 1974, *Astronomy and Astrophysics Supplement*, Vol. 15, p. 417, 15, 417
- Jalal, A., Arvinte, M., Daras, G., et al. 2021, *NeurIPS*
- Jennison, R. 1958, *Monthly Notices of the Royal Astronomical Society*, 118, 276
- Kawar, B., Elad, M., Ermon, S., & Song, J. 2022, in *Advances in Neural Information Processing Systems*
- Kawashima, T., Toma, K., Kino, M., et al. 2021, *The Astrophysical Journal*, 909, 168, doi: [10.3847/1538-4357/abd5bb](https://doi.org/10.3847/1538-4357/abd5bb)
- Kolmogorov, A. N. 1991, *Proceedings of the Royal Society of London. Series A: Mathematical and Physical Sciences*, 434, 9
- Krizhevsky, A., & Hinton, G. 2009, *Learning multiple layers of features from tiny images*, Tech. Rep. 0, University of Toronto, Toronto, Ontario. <https://www.cs.toronto.edu/~kriz/learning-features-2009-TR.pdf>
- Kuramochi, K., Akiyama, K., Ikeda, S., et al. 2018, *The Astrophysical Journal*, 858, 56
- Liu, Z., Luo, P., Wang, X., & Tang, X. 2015, in *Proceedings of International Conference on Computer Vision (ICCV)*
- Lockhart, W., & Gralla, S. E. 2022, *Monthly Notices of the Royal Astronomical Society*, 517, 2462, doi: [10.1093/mnras/stac2743](https://doi.org/10.1093/mnras/stac2743)
- Lu, R.-S., Broderick, A. E., Baron, F., et al. 2014, *The Astrophysical Journal*, 788, 120, doi: [10.1088/0004-637X/788/2/120](https://doi.org/10.1088/0004-637X/788/2/120)
- Luminet, J.-P. 1979, *Astronomy and Astrophysics*, vol. 75, no. 1-2, May 1979, p. 228-235., 75, 228
- Mardani, M., Song, J., Kautz, J., & Vahdat, A. 2023, *arXiv preprint arXiv:2305.04391*
- Medeiros, L., Psaltis, D., Lauer, T. R., & Özel, F. 2023, *The Astrophysical Journal Letters*, 947, L7, doi: [10.3847/2041-8213/acc32d](https://doi.org/10.3847/2041-8213/acc32d)
- Müller, H., & Lobanov, A. 2023, *Astron. Astrophys.*, 672, A26, doi: [10.1051/0004-6361/202244664](https://doi.org/10.1051/0004-6361/202244664)
- Müller, H., Mus, A., & Lobanov, A. 2023, *Astronomy & Astrophysics*, 675, A60
- Nalewajko, K., Sikora, M., & Różańska, A. 2020, *Astronomy & Astrophysics*, 634, A38
- Narayan, R., & Nityananda, R. 1986, *Annual review of astronomy and astrophysics*, 24, 127
- Nemmen, R. 2019, *The Astrophysical Journal Letters*, 880, L26, doi: [10.3847/2041-8213/ab2fd3](https://doi.org/10.3847/2041-8213/ab2fd3)
- Papamakarios, G., Nalisnick, E., Rezende, D. J., Mohamed, S., & Lakshminarayanan, B. 2021, *The Journal of Machine Learning Research*, 22, 2617
- Rogers, A. E., Doeleman, S. S., & Moran, J. M. 1995, *Astronomical Journal (ISSN 0004-6256)*, vol. 109, no. 3, p. 1391-1401, 109, 1391
- Scales, J. A., & Tenorio, L. 2001, *Geophysics*, 66, 389
- Schwab, F. 1984, *Astronomical Journal (ISSN 0004-6256)*, vol. 89, July 1984, p. 1076-1081., 89, 1076
- Schwarz, U. 1978, *Astronomy and Astrophysics*, 65, 345
- Shepherd, M. 2011, *Astrophysics Source Code Library, ascl*
- Sohl-Dickstein, J., Weiss, E., Maheswaranathan, N., & Ganguli, S. 2015, in *International conference on machine learning*, PMLR, 2256–2265
- Song, J., Vahdat, A., Mardani, M., & Kautz, J. 2023, in *International Conference on Learning Representations*. https://openreview.net/forum?id=9_gsMA8MRKQ
- Song, Y., Durkan, C., Murray, I., & Ermon, S. 2021a, in *Thirty-Fifth Conference on Neural Information Processing Systems*
- Song, Y., Shen, L., Xing, L., & Ermon, S. 2022, in *ICLR*. <https://openreview.net/forum?id=vaRCHVj0uGI>
- Song, Y., Sohl-Dickstein, J., Kingma, D. P., et al. 2021b, in *ICLR*. <https://openreview.net/forum?id=PxTIG12RRHS>
- Stein, C. 1972, in *Proc. Sixth Berkeley Symp. Math. Stat. Prob.*, 583–602
- Sun, H., & Bouman, K. L. 2021, in *AAAI*, 2628–2637
- Sun, H., Bouman, K. L., Tiede, P., et al. 2022, *arXiv preprint arXiv:2201.08506*
- Taylor, G. I. 1938, *Proceedings of the Royal Society of London. Series A-Mathematical and Physical Sciences*, 164, 476
- Thompson, A. R., Moran, J. M., & Swenson, G. W. 2017, *Interferometry and synthesis in radio astronomy (Springer Nature)*
- Twiss, R., Carter, A., & Little, A. 1960, *The Observatory*, Vol. 80, p. 153-159 (1960), 80, 153
- van Cittert, P. H. 1934, *Physica*, 1, 201
- van der Schaaf, A., & van Hateren, J. 1996, *Vision Research*, 36, 2759, doi: [https://doi.org/10.1016/0042-6989\(96\)00002-8](https://doi.org/10.1016/0042-6989(96)00002-8)
- Vincent, F., Wielgus, M., Abramowicz, M., et al. 2021, *Astronomy & Astrophysics*, 646, A37
- Walsh, J. L., Barth, A. J., Ho, L. C., & Sarzi, M. 2013, *The Astrophysical Journal*, 770, 86
- Wong, G. N., Prather, B. S., Dhruv, V., et al. 2022, *The Astrophysical Journal Supplement Series*, 259, 64
- Yuan, F., Wang, H., & Yang, H. 2022, *The Astrophysical Journal*, 924, 124, doi: [10.3847/1538-4357/ac4714](https://doi.org/10.3847/1538-4357/ac4714)
- Zernike, F. 1938, *Physica*, 5, 785
- Zhang, C., Bütepage, J., Kjellström, H., & Mandt, S. 2018, *IEEE transactions on pattern analysis and machine intelligence*, 41, 2008